ADVANCING EARTH AND SPACE SCIENCES

JGR Space Physics

RESEARCH ARTICLE
10.1029/2026JA035419

Ray Tracing Method in a General Non-Dipole Magnetic Field

P.-L. Blelly[1,2], J.-F. Ripoll[3,4], A. Dubois[3], R. B. Horne[5], and A. Marchaudon[1,2]

[1]Université de Toulouse, CNES, CNRS, IRAP, Toulouse, France, [2]Ionospheric Research Center IRAP-TASF (IRCIT), Toulouse, France, [3]CEA, DAM, DIF, Arpajon, France, [4]Université Paris-Saclay, CEA, LMCE, Bruyères-le-Châtel, France, [5]British Antarctic Survey, Natural Environment Research Council, Cambridge, UK

Key Points:

- New general mathematical formulation of the Eikonal equations for ray tracing derived for any internal magnetic field model
- We find a tremendous role of the magnetic field model, from a dipole to the full International Geomagnetic Reference Field (IGRF) model for lightning and transmitter frequencies
- Dipole-based rays are often erroneous in path while rays computed with an eccentric-tilted dipole and IGRF can differ with reasonable error

Correspondence to:

P.-L. Blelly and J.-F. Ripoll,
pierre-louis.blelly@irap.omp.eu;
jean-francois.ripoll@cea.fr

Citation:

Blelly, P.-L., Ripoll, J.-F., Dubois, A., Horne, R. B., & Marchaudon, A. (2026). Ray tracing method in a general non-dipole magnetic field. *Journal of Geophysical Research: Space Physics*, *131*, e2026JA035419. https://doi.org/10.1029/2026JA035419

Received 27 MAR 2026
Accepted 18 JUN 2026

Author Contributions:

Conceptualization: P.-L. Blelly, J.-F. Ripoll
Data curation: A. Dubois
Formal analysis: P.-L. Blelly, J.-F. Ripoll, A. Dubois
Funding acquisition: J.-F. Ripoll
Investigation: P.-L. Blelly, J.-F. Ripoll, A. Dubois
Methodology: P.-L. Blelly, J.-F. Ripoll, A. Marchaudon
Project administration: J.-F. Ripoll
Software: P.-L. Blelly, A. Dubois, R. B. Horne
Supervision: P.-L. Blelly, J.-F. Ripoll, R. B. Horne, A. Marchaudon
Validation: P.-L. Blelly, J.-F. Ripoll
Visualization: A. Dubois

Abstract We present a new general mathematical formulation of the Eikonal equations for ray tracing, which can use any internal magnetic field model. The analytical and tractable expressions are conveniently based on a vector formalism, which is independent of any coordinate system. This formalism is newly introduced in the widely used BAS HOTRAY code and tested for frequencies ranging from 1 to 20 kHz, covering lightning and navy transmitter frequencies. We show and quantify the tremendous role of the magnetic field model, testing from the pure dipole field to the full International Geomagnetic Reference Field (IGRF) model. Most often, the longitudinal drift of the rays computed with different geomagnetic models makes a notable difference among them, being absent for rays computed with a pure dipole. The error in path length of the dipole-based rays can be 100% different than the IGRF-based ray. Dipole-based rays are most often drastically erroneous in ray path or final footprint. Rays computed with IGRF or an eccentric-tilted dipole can often agree within a reasonable error range, but not systematically. We find a major importance of the initial wave normal angle and initial azimuthal angle in ray paths. Our study concludes that major ray tracing study should use a realistic magnetic field model to be predictive. Yet, the method remains to be extended to general external magnetic field and more realistic cold plasma density models.

Plain Language Summary In this article, we present a new mathematical formulation of the ray tracing equations, in which the equations are conveniently expressed to handle any magnetic field models, from the simple dipole model to the most advanced International Geomagnetic Reference Field (IGRF) model. This formulation has the specificity to be analytical, vectorial, and general, not relying on any specific coordinate systems. The formalism is newly introduced in a numerical code used in the community for more than four decades. With it, we compute the different trajectories of a ray according to the magnetic field model. We specifically study the propagation of electromagnetic waves, from the ionosphere to the plasmasphere, at wave frequencies generated by lightning in the 1–10 kHz range or by very low frequency (VLF) navy transmitters (within 10–20 kHz). We discuss the important differences found between the use of a dipole field and the use of the IGRF model, so much that they question the common use of a dipole field. Conversely, we find, for instance, a tilted eccentric dipole can sometimes give a first good approximation of the ray path. Our study enlightens and investigates the tremendous effects of the Earth's magnetic field on VLF ray paths.

1. Introduction

Ray tracing is a numerical technique used since the 1960s to study the propagation of a variety of electromagnetic waves evolving in the ionosphere, plasmasphere, and magnetosphere (e.g., Yabroff (1959); Kimura (1966)). For instance, there are many studies computing that way the propagation of whistler-mode chorus waves, listing only the most recent ones (e.g., Bortnik et al., 2011; Bortnik et al., 2009; Bortnik, Thorne, & Meredith, 2007; Bortnik, Thorne, Meredith, & Santolik, 2007; Chen et al., 2009; Colpitts et al., 2020; Crabtree et al., 2012; Feng et al., 2025; Gu et al., 2024; Hanzelka & Santolík, 2019; Hartley et al., 2019; Kang & Bortnik, 2022; Kang et al., 2021; Kang et al., 2024; Kang et al., 2022; Thorne et al., 2010). Ray tracing is commonly used for whistler-mode hiss waves (e.g., Ding et al., 2025; Wu et al., 2024; Yue et al., 2017), exohiss waves(e.g. Ding et al., 2025; Feng et al., 2023; Hanzelka & Santolík, 2019), electromagnetic ion cyclotron waves (e.g., Horne & Thorne, 1993), equatorial noise (e.g., Hanzelka et al., 2022), lightning-generated whistlers (e.g., Cerfolli et al., 2025; Kang & Bortnik, 2022; Starks et al., 2020; Wold et al., 2024; Xia et al., 2024), VLF-transmitter waves (e.g., Gu et al., 2020; Gu et al., 2021; Starks et al., 2020; Usanova et al., 2022; Zhang et al., 2018), electrostatic

Journal of Geophysical Research: Space Physics 10.1029/2026JA035419

Writing – original draft: P.-L. Blelly, J.-F. Ripoll, A. Dubois
Writing – review & editing: P.-L. Blelly, J.-F. Ripoll, A. Dubois, R. B. Horne, A. Marchaudon

electron cyclotron harmonic (ECH) waves (e.g., Horne, 1988; Thorne et al., 2010), magnetosonic waves (e.g., Horne et al., 2000), lower hybrid waves (e.g., Xia et al., 2022), etc.

Among the variety of applications and effects of these studies, ray tracing has been used to characterize wave propagation and consequent wave properties (e.g., Colpitts et al., 2020; Hanzelka et al., 2022; Kang et al., 2021, 2022; Wold et al., 2024; Xia et al., 2024), wave damping (e.g., Bell et al., 2002; Crabtree et al., 2012; Ding et al., 2025; Thorne & Horne, 1994), wave ducting and plume effects (e.g., Bortnik et al., 2011; Chen et al., 2009; Gu et al., 2024; Hanzelka & Santolík, 2019; Inan & Bell, 1977), and wave effects on radiation belt electrons (e.g., Bortnik et al., 2011; Bortnik et al., 2006; Kang & Bortnik, 2022; Kang et al., 2024; Xu et al., 2023). Ray tracing can serve to study the effect of cold plasma density on wave propagation (e.g., Gu et al., 2024) and identify density models (Usanova et al., 2022) which can afterward be applied to any applications such as radiation belt wave particle interactions (e.g., Ripoll, Claudepierre, et al., 2020). About, the capability and accuracy of ray tracing itself, this is, for instance, discussed through similarities and differences found on wave propagation solved with both particle-in-cell (PIC) and ray tracing simulations in Ke et al. (2025).

Ray tracing has contributed to major scientific advances on the whistler-mode chorus wave generation mechanism of plasmaspheric hiss waves (e.g., Bortnik et al., 2008, 2009, 2011; Bortnik, Thorne, & Meredith, 2007; Bortnik, Thorne, Meredith, & Santolik, 2007). Launching more realistic chorus waves with their propagation properties extracted from the Van Allen Probes, Hartley et al. (2019) could show that, although the hiss-chorus generation mechanism is possible, it has a low probability to occur. One important limitation of this theory and the latter results is that they relied on ray tracing simulations done with the use of a pure dipole magnetic field, which drastically influences the propagation path as we will show in this article, for instance, prohibiting longitudinal directions. More generally, waves are traced with ray tracing to find their origin, whether the goal is to explain, for instance, the source of low-altitude hiss in the ionosphere (Chen et al., 2017), how ionospheric lower-hybrid wave could be generated from hiss waves (Xia et al., 2022), or the intrinsic relationship between hiss and exohiss (Ding et al., 2025).

One of the major concerns regarding very low frequency (VLF) ray tracing in the plasmasphere is the background magnetic field. Indeed, all the ray tracing codes consider static curl-free magnetic fields, either simply dipolar (centered on eccentric) of more complex like the International Geomagnetic Reference Field (IGRF) thirteenth Generation magnetic field model (Alken et al., 2021). These formulations only describe the internal contribution to the field as the external contributions resulting form currents in the magnetosphere are discarded $\left(\vec{\nabla} \times \vec{B} = \vec{0} = \mu_0 \vec{J}\right)$. Actually, most ray tracing codes use a dipolar field, even though the effect of the magnetic field is well recognized as major (e.g., Ke et al., 2022; Reid et al., 2022; Usanova et al., 2022; Yue et al., 2017). Computations from the Stanford VLF code (e.g., Reid et al., 2022; Usanova et al., 2022; Wold et al., 2024) are certainly convincing in terms of showing the effect of the magnetic field on the wave trajectory. For instance, Usanova et al. (2022) use the IGRF thirteenth Generation magnetic field model (Alken et al., 2021). Their results will be used and compared with the ones of this article in Section 4.5. Other codes such as the one of the US AFRL (e.g., Starks, 2002; Starks et al., 2008, 2020) and of the NRL (e.g., Crabtree et al., 2012; Ganguli et al., 2019) project their results onto non dipole fields. In Starks et al. (2020) (see their appendix A), a tilted, offset dipole magnetic field, allows them to easily evaluate the L-shell value. The NRL code propagates the rays in a dipole field but can use density values computed from the SAMI3 code (e.g., Huba et al., 2008), itself using a close approximation of the IGRF model for computing the density (Ganguli et al., 2019). Ke et al. (2022) implemented rescaled dipole magnetic fields to study the effect of the magnetic field, though without being able to connect their findings with a realistic magnetic field. Finally (Kang et al., 2021), coded the use of the T89 external magnetic field model Tsyganenko (1989) in a new ray tracing python code, PyRay. None of the aforementioned studies explain the derivation of the necessary mathematical expressions to use a non dipole field.

The British Antarctic Survey (BAS) HOTRAY (Horne, 1989) has been used over the past 40 years for numerous applications such as lightning-generated wave propagation (e.g., Thorne & Horne, 1994; Xia et al., 2024), EMICs propagation (Horne & Thorne, 1993), chorus and ECH propagation including O and Z mode waves (e.g., Horne, 1988), the chorus-to-hiss generation mechanism (Bortnik et al., 2011; Hartley et al., 2019), density effects on chorus propagation (e.g., Chen et al., 2009; Gu et al., 2024), source of low latitude hiss waves (Chen et al., 2017), active experiments (Cerfolli et al., 2025), active wave heating from the ground by EMIC waves (Robinson et al., 2000), navy VLF-transmitter wave propagation (e.g., Gu et al., 2021; Zhang et al., 2018), ionospheric wave populated from the plasmasphere (Xia et al., 2022), effect of interplanetary shocks on whistler-mode wave (Yue et al., 2017), etc. HOTRAY has been applied to other planets as well, such as Jupiter in Mei et al. (1992). HOTRAY has been adapted to use the IGRF model in Zhang et al. (2018) and to use an external magnetic field model in Yue et al. (2017). In these studies, no mathematical details are given on the method. We will show here that the current mathematical formulation of HOTRAY is intrinsically limited to a pure dipole field. Its adaptation for handling a non dipole field involves non-straightforward mathematical developments that will be presented here.

In fact, regardless of the ray tracing code, the reference frame is chosen first, and then the equations are derived in that frame, particularly the gradients associated with the magnetic field. In the case of a simple formulation of the field, analytical expressions are used for the gradients, but in the case of a more complex description, these gradients are computed numerically. The result of such an approach is that these codes are constrained by the initial representation, and consequently, any evolution is hampered by this choice. In this article, we derive, for the first time, a formal and analytical description of ray-tracing equations based on the Eikonal approach, which highlights the key role of the magnetic field. These equations are independent from any coordinate system and consider any curl-free geomagnetic field model. Thanks to the work done by Resseguier et al. (2026), analytical expressions of the magnetic field and its various gradients are derived for any coordinate system, from the simple dipole model to the most advanced IGRF model Alken et al. (2021). This formalism, newly integrated in HOTRAY, is used to compute the different trajectories of a given ray according to the magnetic field model. We discuss the important differences found between the use of a dipole field and the use of the IGRF model, with variations in longitude that are impossible to capture with a simple dipolar magnetic field model. Implications on the ray propagation of waves emitted from the navy VLF transmitters are also discussed.

A motivation of this study is the application of ray tracing to active experiments, which consist in generating and monitoring large scale artificial signals, possibly causing significant disturbances of the ionosphere or the near-Earth space (e.g., Gombosi et al. (2017)). Active experiments can involve chemical release (e.g., (Ganguli et al., 2015)), heating from high-power high-frequency ground transmitters (e.g., (Starks, 2002)), electromagnetic wave emission directly from space or electron beam emission from the ionosphere (e.g., (Reeves et al., 2020)) or space (e.g., (Borovsky & Delzanno, 2019)). These experiments are a method of understanding the electromagnetic environment, its response to man-made external forcing, wave propagation in a disturbed environment and, more generally, wave-particle interactions. In such experiments, the influence of the magnetic field on the wave propagation is major to the point that it is hard to predict accurately the location, strength, and geographic extent of the electromagnetic effects without using the IGRF magnetic field model. Ray tracing is particularly useful for computing the width of the experiment spread and effects (e.g., Cerfolli et al., 2025; Ganguli et al., 2019; Reid et al., 2022; Starks, 2002). For the simulation of these experiments, the realism of the magnetic field geometry is essential to properly compute the dynamic expansion of the experiment. One way to achieve these predictions is with improved and realistic ray tracing methods as we develop in this article using HOTRAY.

The remainder of the paper is organized as follows. Section 2 is devoted to the derivation of the ray tracing equation for a general magnetic field. The demonstration is broken into a few subsections to introduce the geometry and define the various gradients. Section 3 is devoted to the numerical implementation and changes in HOTRAY. We demonstrate in Section 4 the tremendous effect of the geomagnetic field in a simple comprehensive manner, enlightening the large variety of propagation trajectories that each magnetic field model produces. Two types of wave frequencies are treated, both emitted from the ionosphere, LGW waves and VLF-transmitter waves for 3 magnetic field models: a pure dipole, a tilted eccentric dipole (ECT), and the IGRF (Version 13) Alken et al. (2021).

2. Mathematical Formulation

2.1. Ray Tracing Equations

With the use of the Eikonal approximation of geometric optics, the propagation of a wave is given by the system of two equations

$$\begin{cases} \dfrac{d\vec{r}}{dt} = -\vec{\nabla}_{\vec{k}} D \Big/ \dfrac{\partial D}{\partial \omega} \\ \dfrac{d\vec{k}}{dt} = -\vec{\nabla}_{\vec{r}} D \Big/ \dfrac{\partial D}{\partial \omega} \end{cases} \tag{1}$$

with $\vec{r}$ the position, D the dispersion relation, $\vec{k}$ the wave vector, ω the wave frequency and t is the group time (Suchy, 1981). The indices $\vec{k}$ and $\vec{r}$ characterize the quantities with respect to which the gradients are computed. The dispersion relation depends on the position, the wave vector, the magnetic field $\vec{B}$ and the local plasma concentrations $n_{i,e}(\vec{r})$ of the electrons and ions of the environment, that is, the ionosphere, plasmasphere or magnetosphere. The local spatial gradients of density and magnetic field contribute to the spatial gradient of D. The wave vector can be written in a Cartesian coordinate system $(\vec{I}, \vec{J}, \vec{K})$ as

$$\vec{k} = k_x \vec{I} + k_y \vec{J} + k_z \vec{K} \tag{2}$$

In System (1), the wave vector is solved in a Lagrangian coordinate system so that its components (k_x, k_y, k_z) depend only on time. There is no spatial gradient associated with its components, as the components do not depend explicitly on position. This is the fundamental difference between the Lagrangian approach, which follows particles, and the Eulerian approach, which describes the particle trajectory. However, $\vec{k}$ contributes to the spatial gradient of D through its orientation relative to the magnetic field. The orientation of $\vec{k}$ is a position-dependent function.

Let us define $\vec{b}$ as the unit vector parallel to the magnetic field $\vec{B}$ and in the same direction as $\vec{B}$ such that $\vec{b} = \vec{B}/B$ where B is the magnitude of the magnetic field. At a point P in the space through which the ray passes and using the Gram-Schmidt process (Schmidt, 1907), the wave vector can be expressed as

$$\vec{k} = k_{\|} \vec{b}_{\|} + k_{\perp} \vec{b}_{\perp} = \vec{k}_{\|} + \vec{k}_{\perp} \tag{3}$$

where $\vec{b}_{\|}$ and $\vec{b}_{\perp}$ formally stand for the two consecutive vectors of the orthogonalization process and trivially write:

$$\begin{cases} \vec{b}_{\|} = \vec{b} \\ \vec{b}_{\perp} = \dfrac{\vec{k} - (\vec{k}\cdot\vec{b})\,\vec{b}}{\|\vec{k} - (\vec{k}\cdot\vec{b})\,\vec{b}\|} \end{cases} \tag{4}$$

and

$$\begin{cases} k_{\|} = \vec{k} \cdot \vec{b} \\ k_{\perp} = \|\vec{k} - (\vec{k}\cdot\vec{b})\,\vec{b}\,\| \end{cases} \tag{5}$$

Figure 1 shows the wave vector and its parallel and perpendicular components with respect to the magnetic field represented by its unit vector $\vec{b}$.

2.2. Gradients of the Dispersion Relation

The two components $k_{\|}$ and $k_{\perp}$ play a role in the dispersion relation, and D is therefore the multivariable function defined as follows

$$D = D\big(n_{i,e}(\vec{r}), B(\vec{r}), k_{\|}(\vec{r}), k_{\perp}(\vec{r})\big) \tag{6}$$

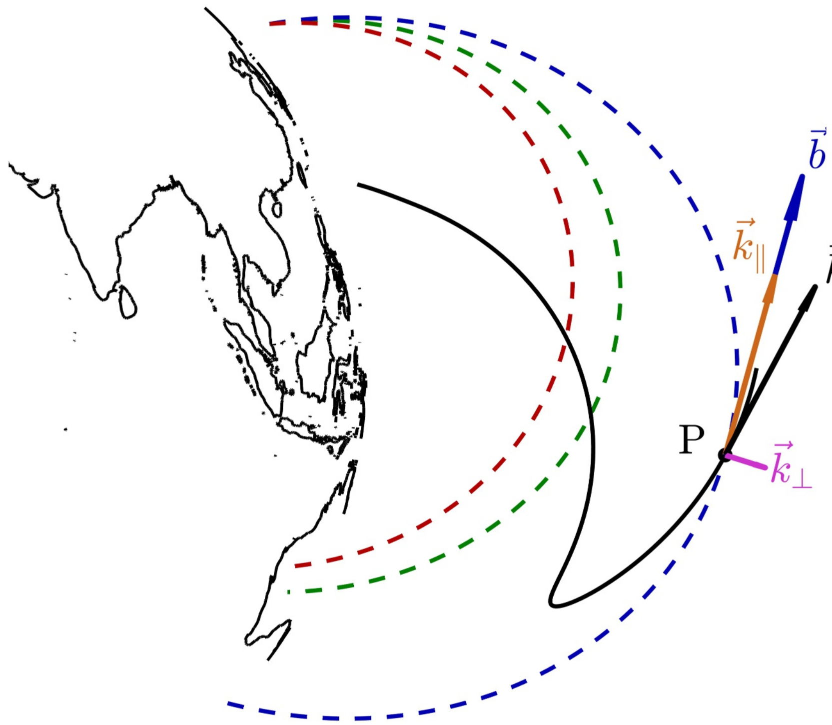

Figure 1. Geometry of wave propagation relative to the magnetic field. The wave vector $\vec{k}$ is shown along with its vector decomposition into components parallel $(\vec{k}_{\parallel})$ and perpendicular $(\vec{k}_{\perp})$ to the magnetic field (represented by its unit vector $\vec{b}$). Three different magnetic field lines are represented: (blue) centered dipole; (red) eccentric, tilted dipole; and (green) International Geomagnetic Reference Field, illustrating variations in magnetic geometry. A (black) single ray path of a 1 kHz wave is partially shown, for the pure dipole model, to indicate the direction of wave propagation relative to the corresponding magnetic field configuration.

where B appears in the definition of the gyrofrequencies.

Using Equation 6 and the chain rule, the gradients of D with respect to $\vec{k}$ and $\vec{r}$ are written

$$\begin{cases} \vec{\nabla}_{\vec{k}} D = \dfrac{\partial D}{\partial k_{\parallel}} \vec{\nabla}_{\vec{k}} k_{\parallel} + \dfrac{\partial D}{\partial k_{\perp}} \vec{\nabla}_{\vec{k}} k_{\perp} \\ \vec{\nabla}_{\vec{r}} D = \displaystyle\sum_{s=i,e} \dfrac{\partial D}{\partial n_s} \vec{\nabla}_{\vec{r}} n_s + \dfrac{\partial D}{\partial B} \vec{\nabla}_{\vec{r}} B + \dfrac{\partial D}{\partial k_{\parallel}} \vec{\nabla}_{\vec{r}} k_{\parallel} + \dfrac{\partial D}{\partial k_{\perp}} \vec{\nabla}_{\vec{r}} k_{\perp} \end{cases} \tag{7}$$

In the following, when the index is omitted, it corresponds to a spatial gradient, that is, with respect to $\vec{r}$. We will not elaborate on the concentration gradients, which are provided by the plasmaspheric model, and will only focus on the magnetic field dependency, and express the gradients of $k_{\parallel}$ and $k_{\perp}$ present in Equation 7.

2.2.1. Gradients of the Wave Vector Components With Respect to the Wave Vector

Let us determine the gradients of $k_{\parallel}$ and $k_{\perp}$ with respect to $\vec{k}$. We have

$$\vec{\nabla}_{\vec{k}} \left(\vec{k} \cdot \vec{k} \right) = 2\vec{k} = \vec{\nabla}_{\vec{k}} \left(k_{\parallel}^2 + k_{\perp}^2 \right) = 2 \left(k_{\parallel} \vec{\nabla}_{\vec{k}} k_{\parallel} + k_{\perp} \vec{\nabla}_{\vec{k}} k_{\perp} \right) \tag{8}$$

which gives

$$\vec{k} = k_{\parallel} \vec{\nabla}_{\vec{k}} k_{\parallel} + k_{\perp} \vec{\nabla}_{\vec{k}} k_{\perp} \tag{9}$$

Thus, by identifying with Equation 3, we obtain the expressions for the gradients of $k_{\|}$ and $k_{\perp}$ with respect to $\vec{k}$

$$\begin{cases} \vec{\nabla}_{\vec{k}} k_{\|} = \vec{b} = \vec{b}_{\|} \\ \vec{\nabla}_{\vec{k}} k_{\perp} = \vec{b}_{\perp} \end{cases} \tag{10}$$

System (10) is a remarkable property.

2.2.2. Gradients of the Wave Vector Components With Respect to the Position

Let us determine the gradients of $k_{\|}$ and $k_{\perp}$ with respect to $\vec{r}$.

From Equation 5, we have

$$\begin{cases} \vec{\nabla}_{\vec{r}} k_{\|} = \vec{\nabla}\left(\vec{k}\cdot\vec{b}\right) = \left(\vec{\nabla}\vec{k}\right)\cdot\vec{b} + \left(\vec{\nabla}\vec{b}\right)\cdot\vec{k} \\ \vec{\nabla}_{\vec{r}} k_{\perp} = \vec{\nabla}\left(\vec{k}\cdot\vec{b}_{\perp}\right) = \left(\vec{\nabla}\vec{k}\right)\cdot\vec{b}_{\perp} + \left(\vec{\nabla}\vec{b}_{\perp}\right)\cdot\vec{k} \end{cases} \tag{11}$$

Using Equation 2 and since k_x, k_y, and k_z do not depend on position, we have $\vec{\nabla}\vec{k} = \underline{\underline{0}}$. This allows us to simplify Equation 11 to

$$\begin{cases} \vec{\nabla}_{\vec{r}} k_{\|} = \left(\vec{\nabla}\vec{b}\right)\cdot\vec{k} \\ \vec{\nabla}_{\vec{r}} k_{\perp} = \left(\vec{\nabla}\vec{b}_{\perp}\right)\cdot\vec{k} \end{cases} \tag{12}$$

After some algebra detailed in Appendix B, we find the gradients of $k_{\|}$ and $k_{\perp}$ with respect to position can be written as

$$\begin{cases} \vec{\nabla}_{\vec{r}} k_{\|} = k_{\perp}\left(\dfrac{\vec{\nabla}\vec{B}}{B}\right)\cdot\vec{b}_{\perp} \\ \vec{\nabla}_{\vec{r}} k_{\perp} = -k_{\|}\left(\dfrac{\vec{\nabla}\vec{B}}{B}\right)\cdot\vec{b}_{\perp} \end{cases} \tag{13}$$

2.2.3. Gradients of the Dispersion Relation With Respect to the Wave Vector

Now that we have the expressions for the gradients of the wave vector components, we can substitute them into System (7).

According to Equation 10, the gradient of D with respect to $\vec{k}$ can be written as

$$\vec{\nabla}_{\vec{k}} D = \frac{\partial D}{\partial k_{\|}}\vec{\nabla}_{\vec{k}} k_{\|} + \frac{\partial D}{\partial k_{\perp}}\vec{\nabla}_{\vec{k}} k_{\perp} = \frac{\partial D}{\partial k_{\|}}\vec{b} + \frac{\partial D}{\partial k_{\perp}}\vec{b}_{\perp} \tag{14}$$

Now, according to Equations 4 and 5, $\vec{b}_{\perp} = (\vec{k} - k_{\|}\vec{b})/k_{\perp}$. Therefore, the gradient of D with respect to $\vec{k}$ is given by

$$\vec{\nabla}_{\vec{k}} D = \left(\frac{\partial D}{\partial k_{\|}} - \frac{k_{\|}}{k_{\perp}}\frac{\partial D}{\partial k_{\perp}}\right)\vec{b} + \frac{1}{k_{\perp}}\frac{\partial D}{\partial k_{\perp}}\vec{k} \tag{15}$$

2.2.4. Gradients of the Dispersion Relation With Respect to the Position

We now derive the gradient of D with respect to $\vec{r}$. Using Equation B8, we have

$$\frac{\partial D}{\partial k_{\parallel}}\vec{\nabla}_{\vec{r}}k_{\parallel} + \frac{\partial D}{\partial k_{\perp}}\vec{\nabla}_{\vec{r}}k_{\perp} = \left(\frac{\partial D}{\partial k_{\parallel}} - \frac{k_{\parallel}}{k_{\perp}}\frac{\partial D}{\partial k_{\perp}}\right)\left(\frac{\vec{\nabla}\vec{B}}{B}\right)\cdot\left(k_{\perp}\vec{b}_{\perp}\right)$$
$$= \left(\frac{\partial D}{\partial k_{\parallel}} - \frac{k_{\parallel}}{k_{\perp}}\frac{\partial D}{\partial k_{\perp}}\right)\left(\frac{\vec{\nabla}\vec{B}}{B}\right)\cdot\left(\vec{k} - k_{\parallel}\vec{b}\right) \quad (16)$$

Using $\vec{\nabla}B = \left(\vec{\nabla}\vec{B}\right)\cdot\vec{b}$ (Equation A5), we finally conclude:

$$\vec{\nabla}_{\vec{r}}D = \sum_{s=i,e}\frac{\partial D}{\partial n_s}\vec{\nabla}n_s + \left[B\frac{\partial D}{\partial B} - k_{\parallel}\left(\frac{\partial D}{\partial k_{\parallel}} - \frac{k_{\parallel}}{k_{\perp}}\frac{\partial D}{\partial k_{\perp}}\right)\right]\frac{\vec{\nabla}B}{B}$$
$$+ \left(\frac{\partial D}{\partial k_{\parallel}} - \frac{k_{\parallel}}{k_{\perp}}\frac{\partial D}{\partial k_{\perp}}\right)\left(\frac{\vec{\nabla}\vec{B}}{B}\right)\cdot\vec{k} \quad (17)$$

One recognizes the term $\left(\frac{\partial D}{\partial k_{\parallel}} - \frac{k_{\parallel}}{k_{\perp}}\frac{\partial D}{\partial k_{\perp}}\right)$ in Equation 17 present in Equations 11 and 12 of Horne (1989). The differences in Equation 17 with Horne (1989)'s formulation lie in the presence of the magnetic field gradients, with additionally a simple compact writing. Equations 17 and 15 are a generalization of Horne (1989)'s formulation for which the magnetic field gradients do not naturally appear and are substituted by gradients of angles, which are dependent on the chosen arbitrary coordinate system and expressed for a pure dipole field (Equations 8 and 9 in Horne (1989)). The proposed generalization allows us to use any given magnetic field $\vec{B}$ and to solve the propagation equations knowing $\vec{B}$ and its gradient$\left(\vec{\nabla}\vec{B}\right)$ (omitting discussing the density for now). To the authors' knowledge, Equations 17 and 15 did not exist in the literature. In Appendix C, we derive Equation 16 in the case of a pure centered non-tilted dipole in order to find the expressions of Horne (1989) in the dipole limit.

3. Numerical Approach and Modifications in HOTRAY

We have modified a few procedures to facilitate the use and portability of HOTRAY. First, the NAG computer library of the Adam routine (Horne, 1989; Phillips, 1987) has been replaced by a Runge-Kutta with adaptive stepping of order 4–5 (Press et al., 2007). Second, the NAG computer library of Bessel functions has been replaced by the Netlib library of Bessel functions (Amos, 1974). HOTRAY uses a dipole field which is analytical and hard coded. Based on IGRF model (Alken et al., 2021), truncations of the set of coefficients used in the spherical harmonics expansion allow to derive different dipolar approximations, defining then the possible modes:

- DIP: the centered non tilted dipole is derived using only the first coefficient
- CDT: the centered tilted dipole is derived using only the first three coefficients
- ECT: the eccentric tilted dipole is derived using only the first eight coefficients
- IGRF: the full set of coefficients is used

The code works with the underlying WKB (Wentzel–Kramers–Brillouin), $|1/k(dk/dx)| \ll k$, which means that the change of wavelength over a wavelength should be small (Swanson, 2003). For compatibility with the old version of HOTRAY, the DIP mode may be adjusted with the coefficient 1.0136, to retrieve the original value of the Earth magnetic moment 7.605×10^{15} T.m^3. Both pure dipole models are found to be fully equivalent leading to same results (to machine precision). The Earth radius is defined as $R_E = 6371.2$ km. The modified version of HOTRAY has been tested on various test cases (not shown) and agrees perfectly with the old version. One of the test cases will be discussed in Section (4.4). The numerical data used for ray tracing computations and the simulation results of the study are available in Ripoll and Blelly (2026).

4. Numerical Simulations

The following section is devoted to showing the profound effects of the magnetic field model at different frequencies, from 1 to 20 kHz, for waves emitted in the mid-ionosphere (from 400 to 700 km) at various positions in latitude and longitude on the Earth. Waves of 1 and 5 kHz are in the range of lightning-generated waves (e.g., Ripoll, Farges, et al., 2020). Wave from 10 to 20 kHz are associated with VLF transmitters (Gu et al., 2021;

Usanova et al., 2022). We compare the effects of wave propagation of 3 magnetic field models: the pure centered dipole (DIP, plotted in blue in all figures), the tilted eccentric dipole (ECT, always plotted in red) and the 13th generation of the IGRF (always plotted in green, year 2020 in used) (Alken et al., 2021).

Regarding the magnetic field model, the tilt angle of the magnetic field is only associated to the dipolar representation of the field and is derived from the first three coefficients of the spherical harmonics expansion. As such, the IGRF model has no specific tilt, but the associated dipole (either centered or eccentric) models have a tilt which can be computed from g_{10}, g_{11} and h_{11}. The eccentricity of the magnetic dipole, that is, the distance between the center of the dipole and the center of the Earth, can be computed using the eight first coefficients of the expansion. In the case considered in the article (year 2020 for IGRF), this leads to an ECT model with a tilt of 11.3° and an eccentricity of 593 km. Its center is located at [−396.45, −377.80, 227.73].

4.1. Models and Assumptions

The simulations are carried out under the assumption of a cold plasma, without taking any wave damping into account, using a diffusive equilibrium model for cold plasma density without ducts. The parameter values of the diffusive equilibrium model in use are the night-side density parameters listed in Bortnik et al. (2011) (not repeated here), which are widely used in the literature (e.g. Gu et al., 2021). The propagation time considered is 3 s for the 1 kHz waves (in Section 4.2) and 2 s for the 5 kHz waves (in Section 4.3) and for both transmitters (in Section 4.4 and 4.5). All simulations end either when the propagation time limit is reached, or if the wave radius goes below 1 Earth radius.

There is a caveat in all simulations presented below. In order to compare the effect of the sole magnetic field model, we choose not to change any other parameter, including the cold plasma density. In reality, the density model should also be tilted/eccentric so that the cold plasma follows the guiding trajectory imposed by the magnetic field. Therefore, as we enlighten below the tremendous effect of the magnetic field, our results still suffer from the absence of the density change in HOTRAY. This prevents the simulations from being fully physically realistic. In order to limit this effect as much as possible, we choose to perform simulations at a longitude at which the magnetic field is such that the density is still symmetric with respect to the magnetic equator of a dipole magnetic field. This leads to presenting numerical simulations in the 80–120° longitude range, where are located the alpha and NWC VLF transmitter simulated in Subsection 4.4 and 4.5.

All simulations are run for a given initial wave normal angle, defined at the launch point of the rays with respect to the local magnetic field vector. It is given in the text, Tables, or figure captions. This initial angle has a tremendous effect on the propagation and the trajectory of the wave. According to its value, we define four types of propagation, as follows and illustrated in Figure 2. First, waves can be trapped within the ionosphere and exhibit low-altitude ionospheric reflections (Figure 2a). These waves can travel large distances as no damping model is yet used. Second, waves can follow a parabolic trajectory from their point of emission in the ionosphere, enter the plasmasphere, and travel down toward their conjugate point in the other Earth's hemisphere, where their propagation comes to an end without any reflection (Figure 2b). Third, direct inward propagation is characterized by waves following a diving trajectory from their point of emission at high altitude toward the Earth at lower altitude, where their propagation comes to an end. The altitude of these waves strictly decreases along their path (Figure 2c). The fourth type is outward propagation from the ionosphere to the plasmasphere, which is characterized by waves expanding spatially and exhibiting high-altitude magnetospheric reflections (Figure 2d).

In the following numerical results, we will always represent the rays in the meridional plane with either a perpendicular position of the observer, corresponding with a view angle of 90°, or an observer located at the longitude of the ray and aligned with the meridional plane, corresponding to a view angle of 0°. The first view allows us to characterize differences in latitude while the second shows the longitudinal drift.

4.2. 1 kHz Wave at 120° Longitude

Figure 3 shows the ray tracing for 1 kHz electromagnetic waves for a source located at 120° longitude and at an altitude of 400 km. From top to bottom, the rows correspond to latitudes of +40°, +20°, −20° and −40°. The launch angles of the waves relative to the magnetic field are, from to bottom, 153°, 114°, 54°, and 7°. Simulations are initiated with an azimuthal angle, η, of zero degrees.

10.1029/2026JA035419

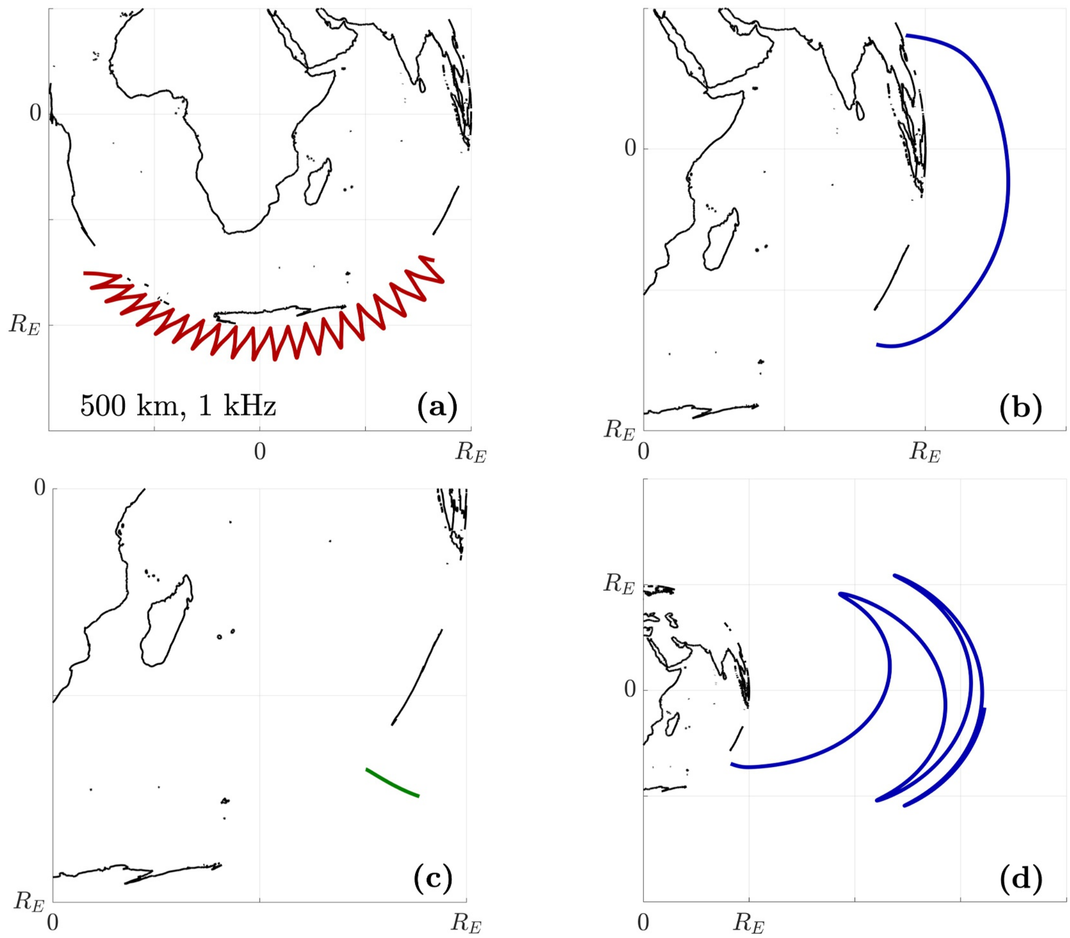

Figure 2. Illustration of the four types of propagation at 1 kHz started at 500 km at (Lat = −40°, Long = 120°). Wave normal angles are (from top left to bottom right) 142°, 8°, 172°, 25°. (a) Ionospheric propagation wave, (b) parabolic propagation wave, (c) earthward propagating wave and (d) outward propagating wave.

All rays that exit the ionosphere follow similarly curved trajectories determined by the dipolar geometry of the magnetosphere, such that each ray travels from one hemisphere to the other, crossing the magnetic equator. It is evident from Figure 3 that, for a given set of geographic coordinates and launch angles, the rays of some geomagnetic field models propagate far within the plasmasphere and undergo multiple magnetospheric reflections, while others directly return to Earth. For instance, for the simulation at −40° latitude, the wave travels outward up to 3.8 R_E in the ECT field and undergoes 3 magnetospheric reflections, while the ray computed with the centered dipole is trapped in the ionosphere and undergoes a single ionospheric reflection.

As expected, significant longitudinal effects can be observed at all latitudes between the pure dipole model and the other two models. Rays from the pure dipole model cannot drift longitudinally and remain highly symmetric around the magnetic equator. For instance, for the rays emitted at +40° latitude (Figure 3a), both the ECT and IGRF rays are distributed on either side of the 120° longitude meridional plane, where the dipole ray travels and stays. This gives a longitudinal drift of about −4° for the ray computed with the ECT model and of about +9° for the one computed with the IGRF model. This difference has to be caused by different field and field gradients as density is unchanged (cf. discussion in Section 5). Both the ECT and IGRF rays remain comparable in minimum latitude, around −12° and maximum latitude, around +40°, and with similar path lengths of 84,500 km for ECT and 84,800 km for IGRF.

Changing the latitude to +20° (Figure 3c), both the dipole and ECT rays stay within the same plane (within 1°) while the ray computed with the IGRF model has a longitudinal drift of +13°. Parabolic propagation occurs only

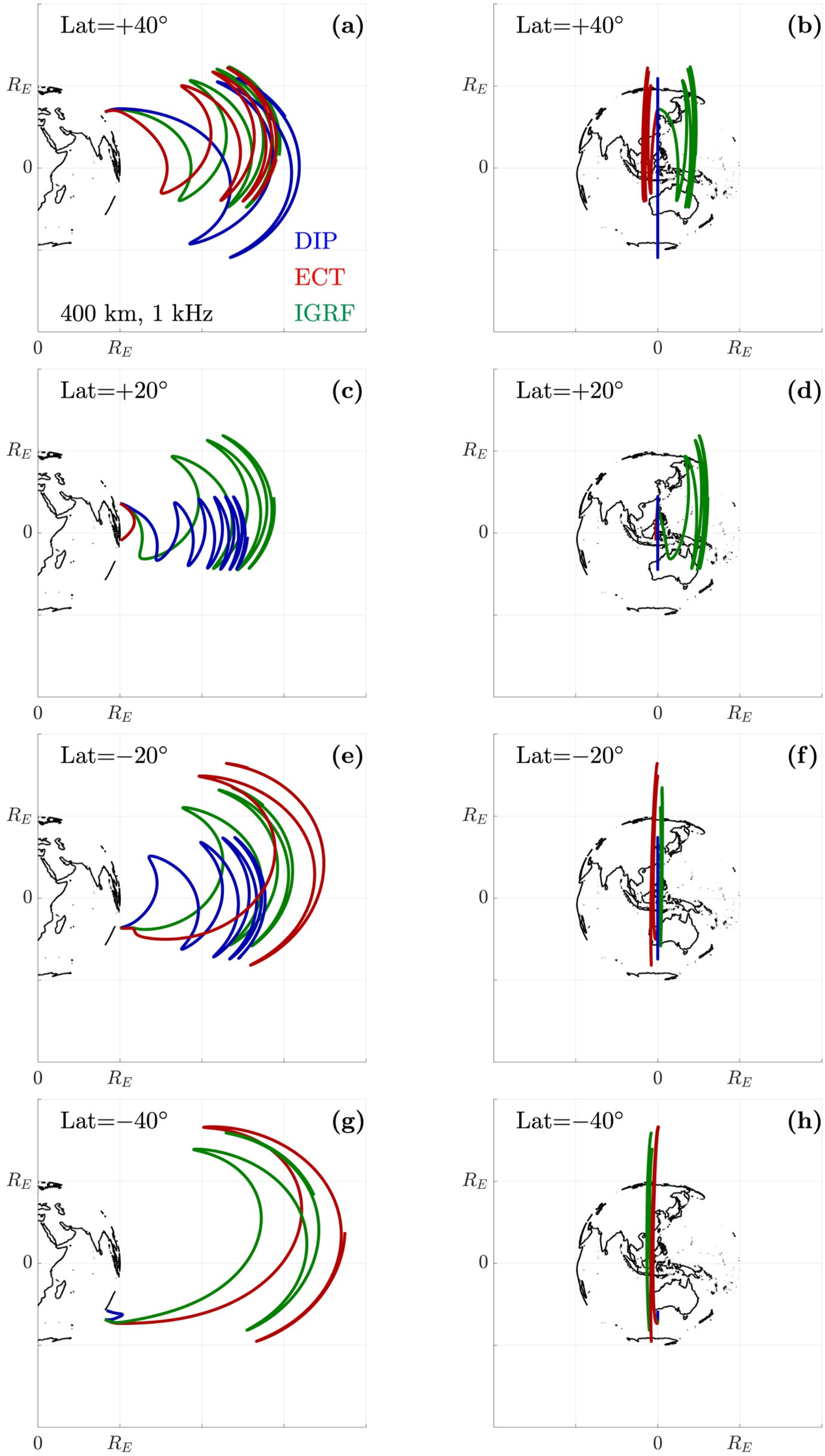

Figure 3. Ray tracing of a 1 kHz wave emitted at 400 km at 120° longitude for different (rows) latitudes and (columns) view angles computed for three magnetic field models (blue) centered dipole, (red) tilted eccentric dipole (ECT), and (green) International Geomagnetic Reference Field. From top to bottom, the latitudes are +40°, +20°, −20°, and −40°. (left column) View angle of 90° (observer perpendicular to the ray) and (right column) a view angle of 0° (observer located at the longitude of the ray) to illustrate the azimuthal propagation.

for the ray computed with the ECT model (Figure 3d). The IGRF path length is 83,600 km, 1.3 times greater than the path length of the dipole ray. The latter reflects 11 times, 1.6 more times than with the IGRF.

At −40° latitude (Figure 3g) the path lengths are 2 780 km, 68,700 km and 75,800 km respectively for the rays computed with the dipole, ECT, and IGRF models. Minimal and maximal latitudes are close to each other for ECT and IGRF rays (within 3°) while the dipole ray reaches only −31° as its maximal latitude.

4.3. 5 kHz Wave at +120° Longitude

Figure 4 shows the ray tracing for 5 kHz electromagnetic waves for the same conditions presented for 1 kHz in the previous section. Overall, rays launched at 1 kHz travel further outward than waves launched at 5 kHz. At 1 kHz, the rays exhibit larger curvatures and greater spreading, whereas the 5 kHz rays are more tightly grouped and shorter. Parabolic propagation is often found at 5 kHz. This happens in all sub-figures of Figure 4, regardless of the magnetic field model. Even for parabolic propagation, differences can be large. For instance, at +20° latitude (Figure 4c), the ECT ray travels over 26° of latitude while the IGRF travels 1.6 times more and the dipole ray about twice as much as with the ECT model. As frequency increases, higher-frequency waves can exceed the lower hybrid frequency, $f_{LH} = \omega_{LH}/2\pi$, defined as

$$\omega_{LH} = \left(\Omega_i^{-1}\Omega_e^{-1} + \omega_{pi}^{-2}\right)^{-1/2}, \tag{18}$$

where $\Omega_i = q_i B/m_i$ is the ion cyclotron pulsation, q_i and m_i are the ion charge and mass, and the subscripts e and i refer to electrons and ions, respectively. When the wave frequency exceeds ω_{LH}, reflection is inhibited, resulting in purely parabolic propagation without reflection.

At −40° latitude (Figure 4g), we find large differences between the various path lengths. The dipole ray travels only 13,800 km while the ECT and IGRF rays travel 68,600 km with 1 reflection for the ECT ray and 83,500 km with 2 reflections for the IGRF ray.

On average, in these simulations, the maximum radius for the 1 kHz waves is around 2.8 R_E, whereas for the 5 kHz waves it is around 1.9 R_E, making it around 68% less for the 5 kHz waves.

The trajectories of the rays using the ECT model often follow more closely those ran with the IGRF model. Both trajectories are quite different from the trajectory computed with the dipole, confirming that the ECT model is a good approximation of the Earth's magnetic field. Though, this comparison may require projecting both ECT and IGRF rays in the same meridional plane. For instance, in Figure 4e, the path length of both the ECT and IGRF waves is comparable, being around 110,000 km for both. Both waves reach the same minimum and maximum latitudes within 3° and reflect 7 times.

Depending on the field model, the wave reaches a given altitude for which it may or may not exceed the lower hybrid frequency and, accordingly, may not or may bounce back. For instance, for the dipole field, in Figures 4e and 4f, the propagation remains parabolic only because the frequency is above the lower hybrid frequency. Interestingly, for the other magnetic field models, the 5 kHz ray propagates to higher L-shells so that 5 kHz remains below the lower hybrid frequency and can bounce.

In general, we find a tremendous effect of the magnetic field model which makes inaccurate tracing waves with a simple dipole field.

4.4. Waves Emitted by the Russian Alpha VLF Transmitter at 11.9 kHz

The Alpha VLF emitter system, also known as RSDN-20, is a Russian system for long-range radio navigation. It consists of three transmitters placed in the proximity of Novosibirsk, Krasnodar, and Khabarovsk (Gu et al., 2020). These transmitters emit multiple frequencies, but we focus on the 11.9 kHz frequency signals emitted by the Novosibirsk transmitter (55.8° latitude, 84.4° longitude).

The conditions of the simulations are slightly changed in this section in order to compare our results to those of Gu et al. (2021). We use an Earth radius of 6,370 km, and a magnetic moment of 8.035×10^{15} T.m^3. Following Gu et al. (2021), we use the full density model described by Bortnik et al. (2011), which combines the night-side diffusive equilibrium model with two identical one sided ducts, increasing the density from the ionosphere to

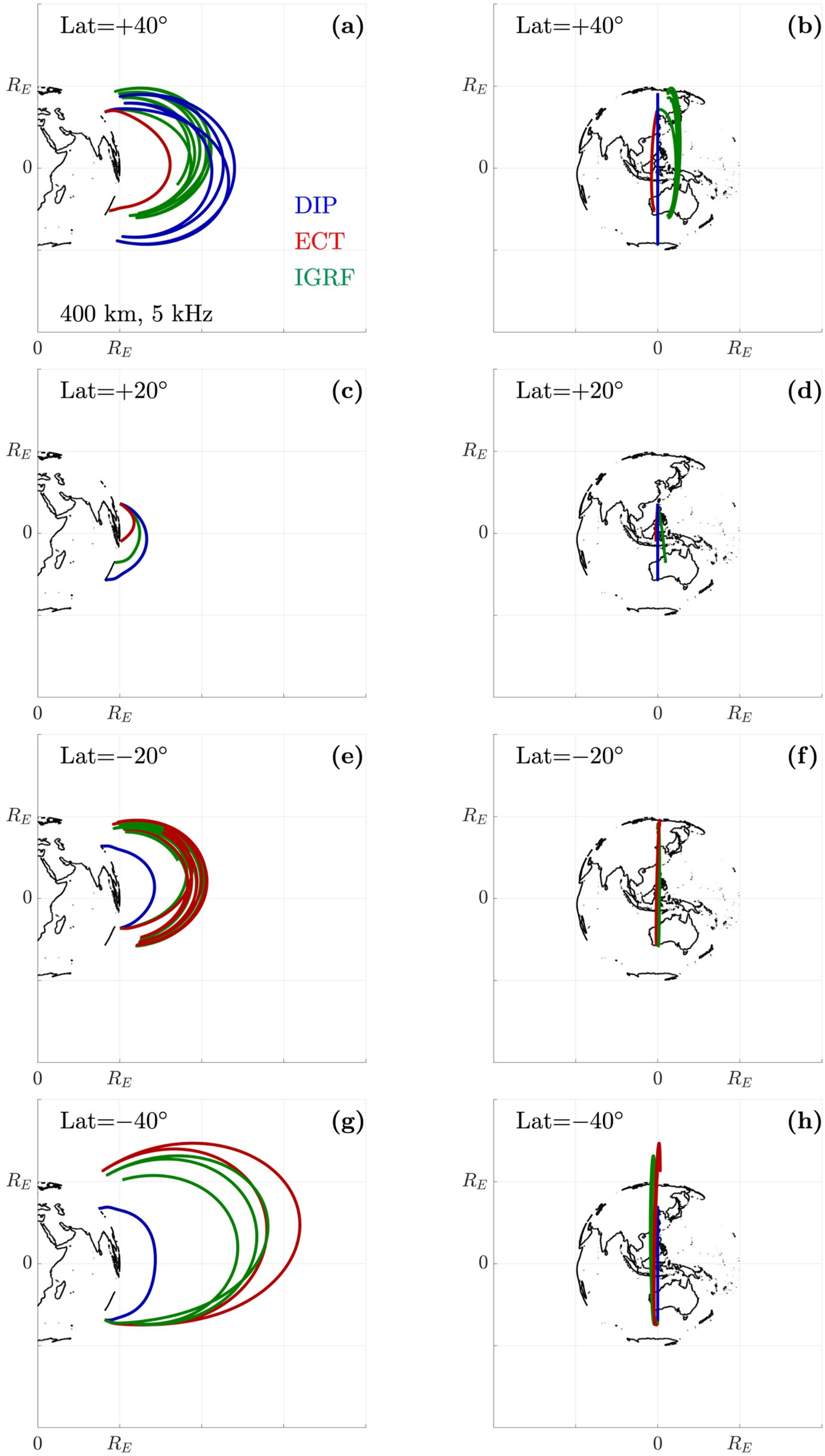

Figure 4. Ray tracing of a 5 kHz wave emitted at 400 km at a longitude of 120° for different latitudes (rows) and view angles (columns), for three magnetic field models: (blue) centered dipole, (red) tilted eccentric dipole, and (green) International Geomagnetic Reference Field. From top to bottom, the latitudes are +40°, +20°, −20°, and −40°. (left column) View angle of 90° (observer perpendicular to the ray) and (right column) a view angle of 0° (observer located at the longitude of the ray) to illustrate the azimuthal propagation.

the plasmasphere. The presence of the two ducts change the results compared with a simulation without ducts and makes this test case more challenging. The simulations are terminated when the radius reaches the imposed limit of 380 km. Simulations are initiated with a wave normal angle of 156.03° and a zero azimuthal angle.

Figure 5a shows the reference solution of Gu et al. (2021) plotted in magenta versus our solution plotted in blue, with perfect overlapping. This simulation is a verification test of the changes made in HOTRAY (cf. Section 3).

In Figures 5b and 5c, we show the rays obtained using both the ECT model and the IGRF model. In these figures, the dipole field solution is manually tilted by 11.3° latitude to match the locations of the rays computed with non-dipole magnetic fields. All the rays in these simulations follow a parabolic trajectory. The longitudes of the terminal point of the rays in the ECT and IGRF models are very similar (within 0.3° of each other) and both lie about 4.5° longitude east of the dipole-model ray. The path length is one of the main distinctions between these rays. The IGRF model leads to a ray with a path length of approximately 32,600 km, which is about 10% longer than the ray path obtained with the pure dipole and 14% longer than the ray path obtained with the ECT model. Interestingly, the latitudes of both the rays computed with the ECT and IGRF model end up close to the ray computed with the dipole, differing by less than 1°. We show in the next section that this is not the case for other transmitters or/and other conditions.

4.5. Waves Emitted by the NWC VLF Transmitter

The NWC transmitter, situated at North West Cape, Australia (21.82°S, 114.17°E), operates at a frequency of 19.8 kHz. It is one of the most powerful VLF transmitters in the world and the most powerful in the Southern Hemisphere. The NWC transmitter is used for long range communications with military submarines (e.g., (Němec et al., 2020)). The NWC transmitter has previously been observed to pitch-angle scatter electrons with energies from 30 to 400 keV (Sauvaud et al., 2008) as well as from 500 keV up to 800 keV (Cunningham et al., 2020), creating enhanced fluxes measured by low-Earth orbiting satellites.

In these simulations, the cold plasma density follows the density described in Section 4, corresponding to the night-side diffusive equilibrium from Bortnik et al. (2011). The simulation is initiated at 500 km, regardless whether or not the ray can reach that altitude when emitted from the transmitter on the ground. We note that full wave modeling in Usanova et al. (2022) (their Figure 3) shows some power escapes for waves with wave normal angles below 30°. The simulation is terminated at a radial distance of 475 km, consistent with the setup used by Usanova et al. (2022) for comparison purposes discussed below.

Figure 6 shows the results of the simulation for the three magnetic field models and two different initial wave normal angles, 0° and 43°, in order to maximize the effect of the magnetic field. The azimuthal angle is first set to zero. The resulting differences in path lengths, terminal point latitudes, longitudinal drifts, and maximum radii of the rays are summarized in Tables 1. Figure 6 shows the conjugate latitudes for the dipole model are consistently much lower than those of the ECT and IGRF model across all simulated rays. Similarly to the simulations at 11.9 kHz, these simulations at high frequency exhibit only parabolic propagation. We observe a small longitudinal drift from 0.5 to 1.6° for this cases, regardless of the magnetic field model and partly due to a zero azimuthal angle. While the difference in latitude is minor between the rays computed with both the IGRF and ECT models for 43°, the error becomes major at for a zero wave normal angle, with 14° difference in latitude representing a 29% longer path length for the ray computed with the ECT model than the ray computed with the IGRF model. This shows using ECT and IGRF does not always lead to agreement in ray path. Major differences are between the IGRF-based ray path length and the dipole field-based ray path length, the latter being smaller by 42% for zero wave normal angle and by 99% for 43°.

In order to increase longitudinal drift, we now increase the azimuthal angle from 0 to 48° and set the wave normal angle to 20°. Ray propagation results are now plotted in Figure 7, with associated ray characteristics reported in Table 2. The value of 48° is chosen to symbolically move the NWC ray footprint from China to North-Korea, when accurately computed with the IGRF model. Demeter measurements in Figure 2 of Usanova et al. (2022) confirm significant NWC wave power in that region. Both IGRF and ECT model-based rays deviate significantly by 12° from their original footprint with 0° azimuthal angle showing the importance of the latter angle. Therefore, large longitudinal drift effects found in the previous sections for zero azimuthal angle should be assumed to be even stronger for non-zero azimuthal angle, which calls for more systematic parametric study of wave propagation. Conversely, the dipole-based ray shows a weak longitudinal drift response to the azimuthal angle, varying

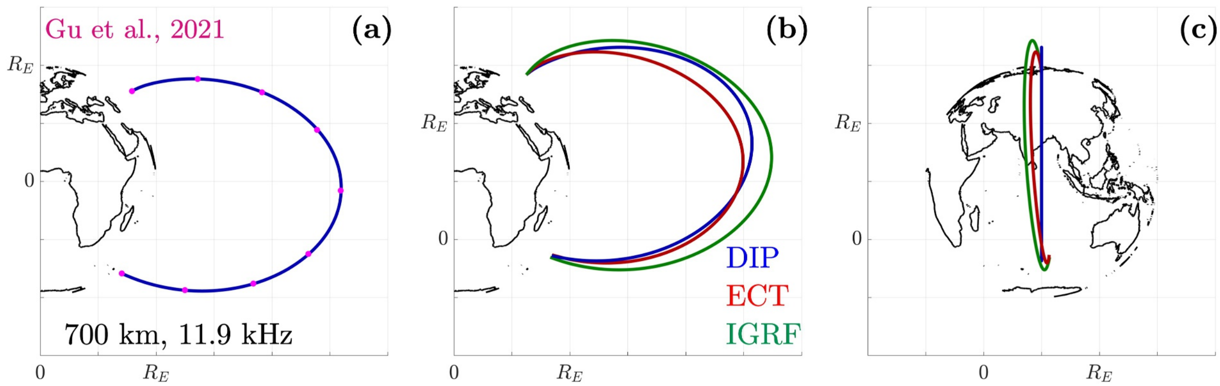

Figure 5. (a) Comparison between (magenta points) Gu et al. (2021)'s solution for one the alpha very low frequency (VLF) transmitter and (blue) our solution, both computed with a centered dipole field. Both simulated rays are emitted at 11.9 kHz, at 700 km, and at 44.5° latitude corresponding to the Novosibirsk VLF transmitter (55.8° latitude, 84.4° longitude). (b) (blue) The dipole ray is now shifted by 11.3° to be comparable with the rays computed with both the (red) ECT and (green) International Geomagnetic Reference Field magnetic field models and launched at Novosibirsk's latitude. All rays are shown with a 90° view angle. Panels (c) same as in (b) but plotted with a view angle of 0°. The initial wave normal angle is 156.03° and the azimuthal angle is zero degrees.

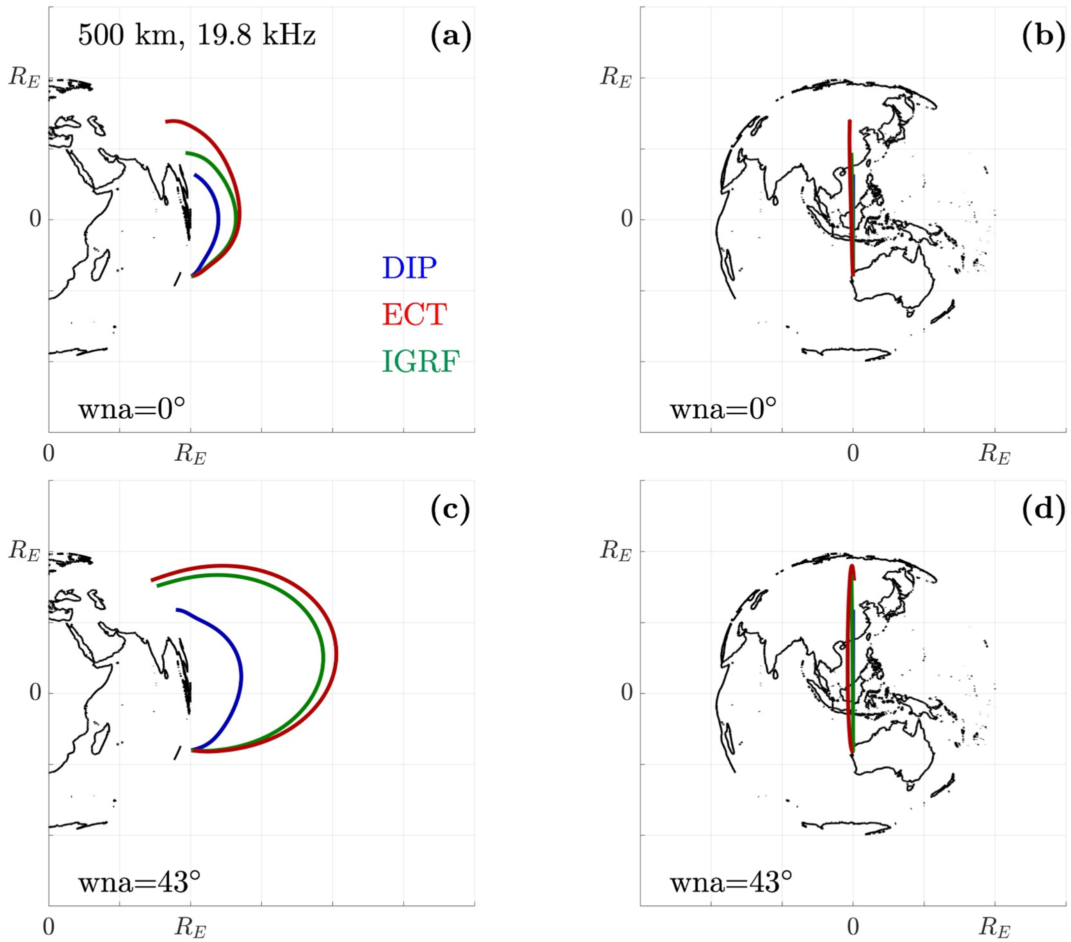

Figure 6. Ray tracing of 19.8 kHz waves emitted at an altitude of 500 km from the NWC very low frequency transmitter for (columns) two different view angles ((a, c) perpendicular and (b, d) aligned). Three magnetic field models are used: (blue) centered dipole, (red) ECT, and (green) International Geomagnetic Reference Field. The initial wave normal angle (wna) are (a, b) 0° and (c, d) 43° with a zero azimuthal angle.

Table 1
Ray Characteristics in Figure 6 With Two Initial Wave Normal Angle of 0° and 43° and Zero Azimuthal Angle, Including Conjugate Latitudes, Longitudinal Drifts, Path Lengths, and Maximum Radii

Model	Angle	Conjugate latitude	Longitudinal drift	Path length	Maximum radius
Centered dipole	(0°,0°)	+17.4°	0°	5,330 km	1.20 R_E
ECT	(0°, 0°)	+40.2°	−1.5°	9,700 km	1.35 R_E
IGRF	(0°,0°)	+26.2°	−0.7°	7,530 km	1.32 R_E
Centered dipole	(43°,0°)	+33.5°	0°	8,830 km	1.36 R_E
ECT	(43°,0°)	+48.0°	−0.5°	19,200 km	2.05 R_E
IGRF	(43°,0°)	+45.0°	−1.6°	17,600 km	1.96 R_E

from 0° to 1.7°. Converted in ray path length, we find the IGRF-based ray travels 32,600 km, which is 14% longer than the ray path obtained with the ECT model. Both ECT and IGRF models thus lead this time to close ray paths. However, the error in path length of the ray computed with the pure dipole model is 85% shorter than the IGRF-based ray path. As in the previous subsections, we confirm the dipole-based rays are always drastically erroneous in ray footprint and path. IGRF- and ECT-based rays can often agree within a reasonable error range, but not systematically. Finally, these results show a major importance of the initial wave normal angle (within 0–50°) and azimuthal angle (within 0–20°), while Usanova et al. (2022) reported that simulations conducted with the initial WNA ± 10 or 20° did not have a major impact on the ray propagation or the ray final location in the conjugate region.

5. Discussions

Although we achieve a new formulation allowing us to integrate the complexity of a general internal magnetic field, this work does not solve for the presence of a general external dynamic magnetic field for which the curl-free relation $\vec{\nabla} \times \vec{B} = \vec{0}$ is no longer satisfied. The curl-free assumption is present in Equation A7 and, thus, in Equation 16, itself used in Equations B2, B8, and 17. This, for instance, limits the extension of this new formulation to ring current region, as it is the case for almost all ray tracing codes.

In the general case, $\vec{\nabla} \times \vec{B} = \vec{0}$ needs to be replaced by $\vec{\nabla} \times \vec{B} = \mu_0 \vec{J}$, in which $\vec{B}$ and $\vec{J}$ now depend upon time, fluctuating at the timescales of the inner magnetosphere. Extension of the present new formalism to the presence of an external field is possible and ongoing. This will be the subject of a future study.

It is possible to obtain Equations 15 and 17 with the use of a fixed well-posed orthogonal coordinate system (not shown and discussed). That demonstration is tenuous. If so, we could not however demonstrate that the final mathematical formulation we reach (composed of System 1 and Equation 15 and Equation 15 is general and valid

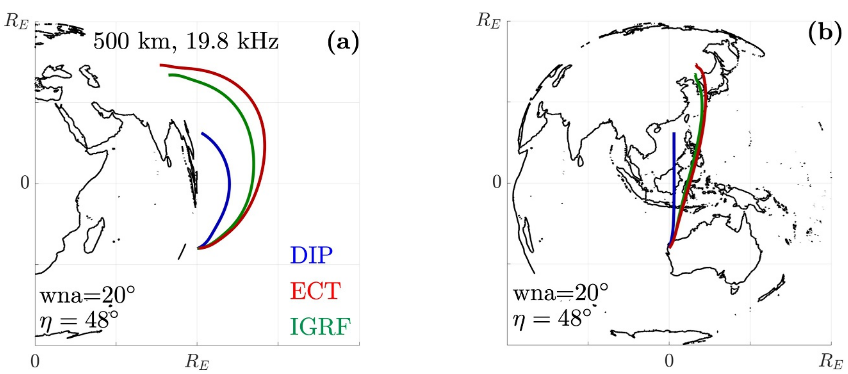

Figure 7. Ray tracing of 19.8 kHz waves emitted at an altitude of 500 km from the NWC very low frequency transmitter for (columns) two different view angles ((a) perpendicular and (b) aligned). Three magnetic field models are used: (blue) centered dipole, (red) tilted eccentric dipole, and (green) International Geomagnetic Reference Field. The initial wave normal angle is 20° with a non-zero azimuth angle of 48°.

Table 2
Ray Characteristics in Figure 7 With an Initial Wave Normal Angle of 20° and an Azimuth Angle of 48°, Including Path Lengths, Conjugate Latitudes, Longitudinal Drifts, and Maximum Radii

Model	Angle	Conjugate latitude	Longitudinal drift	Path length	Maximum radius
Centered dipole	(20°, 48°)	+17.1°	+1.7°	5,350 km	1.20 R_E
ECT	(20°, 48°)	+43.1°	+12.1°	11,300 km	1.47 R_E
IGRF	(20°, 48°)	+38.8°	+10.9°	9,880 km	1.37 R_E

for any coordinate system, contrarily to the present demonstration, for which the vector formalism used throughout the article and the absence of specific coordinate system make it general and always valid.

A caveat of this study is yet not to shift the cold plasma density model with each of the newly introduced magnetic field models, while physically and intrinsically the cold plasma is confined by the non dipolar Earth's magnetic flux tubes. This is deliberately done here for only varying one parameter at a time and assess its importance, here the magnetic field, found to be of major importance. For fully physical simulations, the HOTRAY formulation has to be extended with accounting for the density gradients within a general magnetic field. This task is possible, ongoing, and the subject of a companion study, in which the role of the density and its gradients within a general magnetic field will be assessed and discussed. As we carry the analysis, another goal is to improve the current use of cold plasma density models, so far imposed to be defined in geographic coordinates. Cold plasma density models defined in geographic coordinates are quite limited in the literature, being either based on the commonly used, but approximate and static, diffusive equilibrium formalism, or based on old and sparse satellite measurements. Conversely, numerous and newer cold plasma density models (see review in (Ripoll et al., 2023)) are available in the magnetic coordinate system, such as recent models from the Van Allen Probes and Arase satellites (e.g., (Hartley et al., 2023; Ripoll et al., 2022, 2024)). With this new ray tracing formulation, it now becomes possible to simply use any cold plasma density models and to drastically improve the realism and accuracy of HOTRAY simulations.

Overall, our study shows the capital importance of using an accurate magnetic field for ray propagation in the inner magnetosphere. We suggest revisiting some former studies of importance performed with a pure dipole field. Among them, for instance, the science debate on the mechanism explaining the origin of plasmaspheric hiss from chorus waves source located in the plasma trough (e.g.., (Bortnik et al., 2008, 2011; Hartley et al., 2019)) should be revisited with accounting for a real magnetic field rather than a pure dipole. This requires the use of an external magnetic field above 3 Earth radii, not yet available in our formulation.

6. Conclusions

In this article, we provide a new formulation of the general ray tracing equations based on the Eikonal approximation of geometric optics valid for any magnetic field model. The model is composed of System (1) that is closed with Equation 15 and Equation 17. The equations are analytical and end up to be tractable expressions of the magnetic field gradients, with respect of position and wave vectors, therefore, allowing to implement simply any internal planetary magnetic field models.

The mathematical demonstration has the advantage to be fully defined by vectors and not to depend on a specific coordinate system, making it fully general. The vector form we reach is extremely compact, intuitive, and meaningful. A remarkable property is the simple expression of the wave vector gradients with respect to the wave vector coordinates as a simple function of the parallel and perpendicular magnetic field components (Equation 10). Similarly, the wave vector gradients with respect to position (Equation B8) is simply writable as a vector function of magnetic field gradients. Thus, the simple knowledge of the magnetic field gradients opens up to the computation of any general ray path propagation.

Here, we test a pure dipole, a tilted dipole, an eccentric tilted dipole, and the full IGRF model (Alken et al., 2021). Such ray tracing can be indistinctly used for applications occurring in the Earth's ionosphere, plasmasphere, and magnetosphere, yet as long as the external magnetic field does not dominate the total field. The extension of the present new formalism to the presence of an external field is possible and ongoing.

We show that the formulation converges toward the pure dipole formulation derived in HOTRAY (cf. Appendix C). This attests the correctness of the HOTRAY formulation, but allows to show that Equations 8–10 in Horne (1989) are specific to a dipole field (see Equation C6 in Appendix C). Thus, a non dipole magnetic field model cannot be plugged into HOTRAY equations while keeping Equations 8–10 of Horne (1989).

Implementing the new formulation in the BAS HOTRAY code, we perform a numerical study based on four numerical test cases, two at frequencies of LGW waves and two at frequencies of navy VLF transmitters (i.e., the NWC in Australia and the Alpha transmitter in Russia), all within the range of 1–20 kHz. The tests are dedicated to compare ray paths obtained with a given magnetic field model versus another, as well as to assess how simple models, such as a pure dipole or a tilted/eccentric dipole (ECT) perform in regard to the most accurate model provided by the IGRF model. Our study leaves no doubt in demonstrating a profound influence of the Earth's geomagnetic field on the ray path and ray properties. Ray paths largely differ from one ray to another when the magnetic field model is changed.

When emitting a ray above the dense ionosphere at 500 km, plasmaspheric propagation with multiple bounces occurs mostly at lower frequency (<5 kHz) and is favored by high latitude emission. At low frequency, the ray path in the plasmasphere drastically changes. As the frequency increases to above 5 kHz, the ray path becomes simpler, made of a parabolic trajectory from the emission hemisphere to the other, without any bounce. Initial wave normal angle below 90° lead to waves propagating downward to the ground. Initial wave normal angle above 90° lead to waves propagating upward directly to the opposite Earth's hemisphere. In between, lies ionospheric trapping, made of multiple bounces in the atmosphere-ionosphere wave guide, only happening for initial wave normal angles within the 90° range. In all cases, we find trajectories are drastically different in presence of a dipole field, for which the absence of longitudinal drift causes significant errors in most simulated cases. Furthermore, all (but one) simulated cases had a favorable zero azimuthal angle, limiting longitudinal drift, while non zero azimuthal angle increases even further longitudinal drift and produces even larger errors with a dipole field. The ECT-based and IGRF-based rays path are often close to each other which attests the ECT model is a valid first order approximation. However, we could find some tests for which the ECT-based ray path error was also large compared with IGRF.

Our study demonstrates how difficult it can be to predict the path of a wave traveling within the deep plasmasphere when assuming a dipole field. This may explain why predicted direct wave transmission campaigns from the DSX satellite toward the Arase satellite failed during numerous close conjunctions of the two satellites, ending up with a low success rate of 1 out of 50 (McCollough et al., 2022), and confirming the need of the development of accurate ray tracing models.

Appendix A: Gradient and Curl Properties Applied to the Magnetic Field

Let us prove some properties of the gradient. Let $\vec{A}$ and $\vec{B}$ be two arbitrary vectors. We start from the following equality

$$\vec{\nabla}(\vec{A}\cdot\vec{B}) = (\vec{\nabla}\vec{A})\cdot\vec{B} + (\vec{\nabla}\vec{B})\cdot\vec{A} \tag{A1}$$

If $\vec{A}\cdot\vec{B} = 0$, then using Equation A1

$$(\vec{\nabla}\vec{A})\cdot\vec{B} = -(\vec{\nabla}\vec{B})\cdot\vec{A} \tag{A2}$$

If $\|\vec{A}\| = 1$, then $\vec{\nabla}(\vec{A}\cdot\vec{A}) = \vec{\nabla}(\|\vec{A}\|^2) = 0$. Therefore, using Equation A1

$$2(\vec{\nabla}\vec{A})\cdot\vec{A} = 0 \Rightarrow (\vec{\nabla}\vec{A})\cdot\vec{A} = 0 \tag{A3}$$

The canonical Cartesian basis $(\vec{I}, \vec{J}, \vec{K})$ being fixed, we immediately have

$$\vec{\nabla}\vec{I} = \vec{\nabla}\vec{J} = \vec{\nabla}\vec{K} = \underline{\underline{0}} \tag{A4}$$

From Equation A1, we can write $\vec{\nabla}(B^2) = \vec{\nabla}(\vec{B}\cdot\vec{B}) = 2B(\vec{\nabla}B) = 2(\vec{\nabla}\vec{B})\cdot\vec{B}$, where $\vec{B} = B\vec{b}$ and $B = \|\vec{B}\|$. We can the derive:

$$\vec{\nabla}B = (\vec{\nabla}\vec{B})\cdot\vec{b} \tag{A5}$$

Properties (A2) through (A5) are used in the main text.

Application to the magnetic field: Let us now consider a curl-free magnetic field $\vec{B}$ (i.e., $\vec{\nabla}\times\vec{B} = \vec{0}$), whose magnitude is denoted by B and the associated unit vector by $\vec{b} = \vec{B}/B$. We have:

$$(\vec{\nabla}\vec{B})\cdot\vec{A} = \vec{A}\times(\vec{\nabla}\times\vec{B}) + (\vec{A}\cdot\vec{\nabla})\vec{B}. \tag{A6}$$

that simplifies to

$$(\vec{\nabla}\vec{B})\cdot\vec{A} = (\vec{A}\cdot\vec{\nabla})\vec{B}. \tag{A7}$$

Expanding the remaining term yields

$$(\vec{A}\cdot\vec{\nabla})\vec{B} = (\vec{A}\cdot\vec{\nabla})(B\vec{b}) = [\vec{A}\cdot(\vec{\nabla}B)]\vec{b} + B(\vec{A}\cdot\vec{\nabla})\vec{b} \tag{A8}$$

Now, applying relation (A6) to the unit vector $\vec{b}$

$$(\vec{\nabla}\vec{b})\cdot\vec{A} = \vec{A}\times(\vec{\nabla}\times\vec{b}) + (\vec{A}\cdot\vec{\nabla})\vec{b} \tag{A9}$$

Since $\vec{\nabla}\times\vec{B} = \vec{0}$, we have

$$\vec{\nabla}\times(B\vec{b}) = (\vec{\nabla}B)\times\vec{b} + B(\vec{\nabla}\times\vec{b}) = \vec{0} \tag{A10}$$

from which we can derive the curl of $\vec{b}$

$$\vec{\nabla}\times\vec{b} = \vec{b}\times\left(\frac{\vec{\nabla}B}{B}\right) \tag{A11}$$

For $\vec{A}$, $\vec{B}$ and $\vec{C}$ three arbitrary vectors, we use the following property:

$$\vec{A}\times(\vec{B}\times\vec{C}) = \vec{B}(\vec{A}\cdot\vec{C}) - \vec{C}(\vec{A}\cdot\vec{B}) \tag{A12}$$

Injecting Equation A11 in A9, and using the vector triple product property, we obtain

$$(\vec{\nabla}\vec{b})\cdot\vec{A} = \vec{A}\times\left(\vec{b}\times\frac{\vec{\nabla}B}{B}\right) + (\vec{A}\cdot\vec{\nabla})\vec{b} = \left(\vec{A}\cdot\frac{\vec{\nabla}B}{B}\right)\vec{b} - (\vec{A}\cdot\vec{b})\frac{\vec{\nabla}B}{B} + (\vec{A}\cdot\vec{\nabla})\vec{b} \tag{A13}$$

Using Equation A7, we have:

$$(\vec{A}\cdot\vec{\nabla})\vec{b} = (\vec{A}\cdot\vec{\nabla})\left(\frac{\vec{B}}{B}\right) = \frac{1}{B}(\vec{A}\cdot\vec{\nabla})\vec{B} - \left(\vec{A}\cdot\frac{\vec{\nabla}B}{B}\right)\vec{b} \tag{A14}$$

$$= \frac{\vec{\nabla}\vec{B}}{B}\cdot\vec{A} - \left(\vec{A}\cdot\frac{\vec{\nabla}B}{B}\right)\vec{b} \tag{A15}$$

Finally, this expression can be further simplified using relation (A5), applied to the magnetic field, which reads $\vec{\nabla}B/B = \left(\vec{\nabla}\vec{B}/B\right)\cdot\vec{b}$. We then obtain

$$\left(\vec{\nabla}\vec{b}\right)\cdot\vec{A} = \left(\frac{\vec{\nabla}\vec{B}}{B}\right)\cdot\left[\vec{A} - \left(\vec{A}\cdot\vec{b}\right)\vec{b}\right]. \tag{A16}$$

Note that $\left[\vec{A} - \left(\vec{A}\cdot\vec{b}\right)\vec{b}\right]$ is none other than the vector component of $\vec{A}$ orthogonal to $\vec{b}$ in the plane $\left(\vec{A},\vec{b}\right)$.

Appendix B: Gradients of the Wave Vector With Respect to Position

We start with Equation 12 repeated here

$$\begin{cases}\vec{\nabla}_{\vec{r}}k_{\parallel} = \left(\vec{\nabla}\vec{b}\right)\cdot\vec{k}\\ \vec{\nabla}_{\vec{r}}k_{\perp} = \left(\vec{\nabla}\vec{b}_{\perp}\right)\cdot\vec{k}\end{cases} \tag{B1}$$

Applying Equation A16 to the wave vector $\vec{k}$, the gradient of $k_{\parallel}$ with respect to position can be written as

$$\vec{\nabla}_{\vec{r}}k_{\parallel} = \left(\frac{\vec{\nabla}\vec{B}}{B}\right)\cdot\left[\vec{k} - \left(\vec{k}\cdot\vec{b}\right)\vec{b}\right] = k_{\perp}\left(\frac{\vec{\nabla}\vec{B}}{B}\right)\cdot\vec{b}_{\perp} \tag{B2}$$

By using the decomposition of $\vec{k}$ into $k_{\parallel}$ and $k_{\perp}$ (Equation 3), the gradient of $k_{\perp}$ with respect to position can be written as

$$\vec{\nabla}_{\vec{r}}k_{\perp} = \left(\vec{\nabla}\vec{b}_{\perp}\right)\cdot\left(k_{\parallel}\vec{b} + k_{\perp}\vec{b}_{\perp}\right) = k_{\perp}\left(\vec{\nabla}\vec{b}_{\perp}\right)\cdot\vec{b}_{\perp} + k_{\parallel}\left(\vec{\nabla}\vec{b}_{\perp}\right)\cdot\vec{b} \tag{B3}$$

Now, on one hand, since $\vec{b}_{\perp}$ is a unit vector, Equation A2 gives

$$\left(\vec{\nabla}\vec{b}_{\perp}\right)\cdot\vec{b}_{\perp} = 0 \tag{B4}$$

On the other hand, since by construction $\vec{b}\cdot\vec{b}_{\perp} = 0$, Equation A2 can be written as

$$\left(\vec{\nabla}\vec{b}_{\perp}\right)\cdot\vec{b} = -\left(\vec{\nabla}\vec{b}\right)\cdot\vec{b}_{\perp} \tag{B5}$$

Thus, by using Equations (B4) and (B5), Equation (B3) becomes

$$\vec{\nabla}_{\vec{r}}k_{\perp} = -k_{\parallel}\left(\vec{\nabla}\vec{b}\right)\cdot\vec{b}_{\perp} \tag{B6}$$

which becomes, upon applying Equation A16 to $\vec{b}_{\perp}$,

$$\vec{\nabla}_{\vec{r}}k_{\perp} = -k_{\parallel}\left(\frac{\vec{\nabla}\vec{B}}{B}\right)\cdot\vec{b}_{\perp} \tag{B7}$$

We thus find the gradients of $k_{\parallel}$ and $k_{\perp}$ with respect to position are given by

$$\begin{cases}\vec{\nabla}_{\vec{r}}k_{\parallel} = k_{\perp}\left(\frac{\vec{\nabla}\vec{B}}{B}\right)\cdot\vec{b}_{\perp}\\ \vec{\nabla}_{\vec{r}}k_{\perp} = -k_{\parallel}\left(\frac{\vec{\nabla}\vec{B}}{B}\right)\cdot\vec{b}_{\perp}\end{cases} \tag{B8}$$

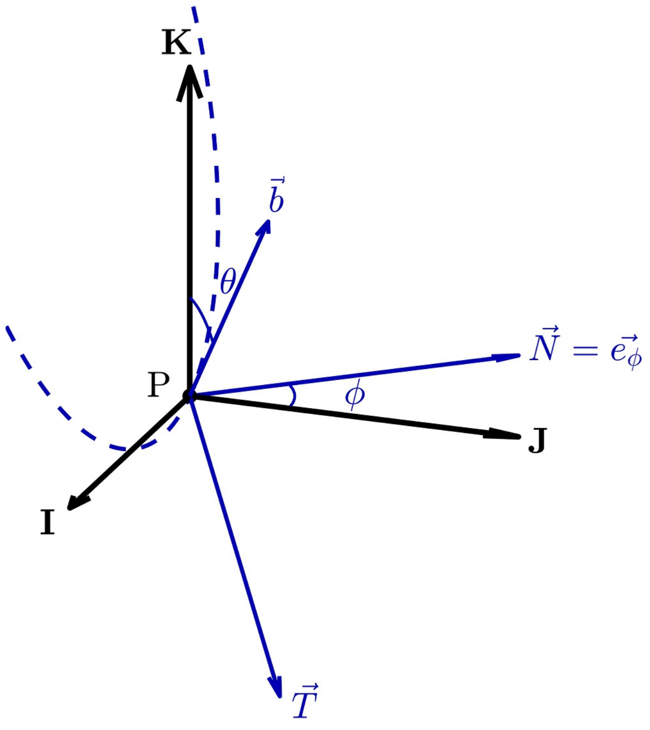

Figure C1. (in blue) Trihedron $(\vec{T},\vec{N},\vec{b})$ and (in black) the Cartesian coordinate frame at a point P located on (dashed line) a magnetic field line.

Appendix C: The Pure Dipole

In this section we derive Equation 16 in the case of a pure centered non-tilted dipole in order to find the limit of Horne (1989). The expression of the magnetic dipole in geocentric coordinate system is $V = -|V_o|\,\frac{\sin\lambda}{r^2}$. Introducing the Cartesian basis $(\vec{I},\vec{J},\vec{K})$, we can derive the dipole magnetic field in this coordinate system:

$$\begin{cases} B_x = -3|V_o|\,\dfrac{xz}{r^5} \\ B_y = -3|V_o|\,\dfrac{yz}{r^5} \\ B_z = -|V_o|\,\dfrac{3z^2 - r^2}{r^5} \end{cases} \tag{C1}$$

with $B = \|\vec{B}\| = \sqrt{B_x^2 + B_y^2 + B_z^2} = |V_0|\sqrt{r^2 + 3z^2}/r^4$. The normalized $\vec{b}$ vector becomes $\vec{b} = -\frac{1}{r\sqrt{r^2+3z^2}}\left(3xz\vec{I} + 3yz\vec{J} + (3z^2 - r^2)\vec{K}\right)$. The tensor $\left(\frac{\vec{\nabla}\vec{B}}{B}\right)$ can be computed and reads

$$\left(\frac{\vec{\nabla}\vec{B}}{B}\right) = -\frac{3}{r^3\sqrt{r^2+3z^2}}\begin{pmatrix} z(r^2-5x^2) & -5xyz & x(r^2-5z^2) \\ -5xyz & z(r^2-5y^2) & y(r^2-5z^2) \\ x(r^2-5z^2) & y(r^2-5z^2) & z(3r^2-5z^2) \end{pmatrix} \tag{C2}$$

Let us introduce the vectors $\vec{N} = \cos\phi\,\vec{J} - \sin\phi\,\vec{I}$ and $\vec{T} = \vec{N}\times\vec{b}$ such that the triplet $(\vec{T},\vec{N},\vec{b})$ forms a local right handed orthogonal basis shown in Figure C1.

In this basis, the wave vector $\vec{k}$ can be written $\vec{k} = k_T\vec{T} + k_N\vec{N} + k_b\vec{b}$. By construction,

$$k_\perp\vec{b}_\perp = k_T\vec{T} + k_N\vec{N}.$$

Equation 16 can therefore be written

$$\frac{\partial D}{\partial k_\parallel}\vec{\nabla}_{\vec{r}}k_\parallel + \frac{\partial D}{\partial k_\perp}\vec{\nabla}_{\vec{r}}k_\perp = \left(\frac{\partial D}{\partial k_\parallel} - \frac{k_\parallel}{k_\perp}\frac{\partial D}{\partial k_\perp}\right)\left(k_T\frac{\vec{\nabla}\vec{B}}{B}\cdot\vec{T} + k_N\frac{\vec{\nabla}\vec{B}}{B}\cdot\vec{N}\right). \tag{C3}$$

Using $\vec{T}$, $\vec{N}$, and $\vec{b}$, we seek $(\vec{\nabla}\vec{B}/B)\cdot\vec{T}$ and $(\vec{\nabla}\vec{B}/B)\cdot\vec{N}$.

Using the expressions of $\vec{T}$, $\vec{N}$, and $\vec{b}$ as functions of (x,y,z), one can now compute

$$\left(\frac{\vec{\nabla}\vec{B}}{B}\right)\cdot\vec{T} = \frac{3(r^2+z^2)}{(r^2+3z^2)\,r^2\sqrt{x^2+y^2}}\begin{pmatrix} xz \\ yz \\ -x^2-y^2 \end{pmatrix} \tag{C4}$$

and

$$\left(\frac{\vec{\nabla}\vec{B}}{B}\right)\cdot\vec{N} = \frac{3z}{r\sqrt{r^2+3z^2}\sqrt{x^2+y^2}}\begin{pmatrix} y \\ -x \\ 0 \end{pmatrix} \tag{C5}$$

Since we have $\vec{\nabla}\theta = -\frac{3(r^2+z^2)}{(r^2+3z^2)\,r^2\sqrt{x^2+y^2}}\left(xz\vec{I} + yz\vec{J} - (x^2+y^2)\vec{K}\right)$ and $\sin\theta\,\vec{\nabla}\varphi = -\frac{3z}{r\sqrt{r^2+3z^2}\sqrt{x^2+y^2}}\left(y\vec{I} - x\vec{J}\right)$, we find that

$$\left(\frac{\vec{\nabla}\vec{B}}{B}\right)\cdot\vec{T} = -\vec{\nabla}\theta, \quad \left(\frac{\vec{\nabla}\vec{B}}{B}\right)\cdot\vec{N} = -\sin\theta\,\vec{\nabla}\phi. \tag{C6}$$

Injecting Eq. (C6) in Equation (C3), we find

$$\frac{\partial D}{\partial k_\parallel}\vec{\nabla}_{\vec{r}}k_\parallel + \frac{\partial D}{\partial k_\perp}\vec{\nabla}_{\vec{r}}k_\perp = \left(\frac{k_\parallel}{k_\perp}\frac{\partial D}{\partial k_\perp} - \frac{\partial D}{\partial k_\parallel}\right)\left(k_T\vec{\nabla}\theta + k_N\sin\theta\vec{\nabla}\phi\right) \tag{C7}$$

which is Equation 10 of Horne (1989) derived for a pure, centered, non-tilted dipole. This confirms the equivalence of the present approach with the one of Horne (1989) for the pure dipole.

Conflict of Interest

The authors declare no conflicts of interest relevant to this study.

Availability Statement

The numerical data used for ray tracing computations and the simulation results of the study are available at Zenodo via the zenodo link 10.5281/zenodo.20276172 with Creative Commons Attribution 4.0 International licence (Ripoll & Blelly, 2026).

Acknowledgments

PLB, JFR, AM, and AD acknowledge the support the AID (Agence de l'Innovation et de la Defense) of the Direction Générale de l'Armement (DGA) and the French ANR (Agence Nationale de la Recherche), under Grant ANR-22-ASTR-0009-01 (Project ANR ASTRID PACTE-ESPACE). RBH was supported by Natural Environment Research Council (NERC) Grant NE/Y006178/1 PRESCIENT (2024–2028). JFR research was partly supported by the International Space Science Institute (ISSI) in Bern through ISSI International Team project 25–635 ″ Energization processes of the ionospheric plasmas across the magnetosphere" led by J. Dargent. This work is supported by the Action Thématique Soleil Terre (ATST) from Institut des Sciences de l'Univers of Centre National de la Recherche Scientifique (INSU/CNRS) co-funded by Centre National d'Etudes Spatiales (CNES) and CEA. This work was granted access to the HPC resources of CALMIP supercomputing center under the allocation 2025-P1520 and of Très Grand Centre de Calcul (TGCC) of the Commissariat à l'Énergie Atomique et aux Énergies Alternatives (CEA). Open access publication funding provided by COUPERIN CY26.

References

Alken, P., Thébault, E., Beggan, C. D., Amit, H., Aubert, J., Baerenzung, J., et al. (2021). International geomagnetic reference field: The thirteenth generation. *Earth Planets and Space*, *73*(1), 49. https://doi.org/10.1186/s40623-020-01288-x

Amos, D. E. (1974). Computation of modified bessel functions and their ratios. *Mathematics of Computation*, *28*(125), 239–251. Retrieved 2026-02-11, from. https://doi.org/10.1090/s0025-5718-1974-0333287-7

Bell, T. F., Inan, U. S., Bortnik, J., & Scudder, J. D. (2002). The Landau damping of magnetospherically reflected whistlers within the plasmasphere. *Geophysical Research Letters*, *29*(15), 23-1. https://doi.org/10.1029/2002GL014752

Borovsky, J. E., & Delzanno, G. L. (2019). Active experiments in space: The future. *Frontiers in Astronomy and Space Sciences*, *6*, 31. https://doi.org/10.3389/fspas.2019.00031

Bortnik, J., Chen, L., Li, W., Thorne, R. M., & Horne, R. B. (2011). Modeling the evolution of chorus waves into plasmaspheric hiss. *Journal of Geophysical Research: Space Physics*, *116*(A8). https://doi.org/10.1029/2011JA016499

Bortnik, J., Inan, U. S., & Bell, T. F. (2006). Temporal signatures of radiation belt electron precipitation induced by lightning-generated mr whistler waves: 1. Methodology. *Journal of Geophysical Research: Space Physics*, *111*(A2). https://doi.org/10.1029/2005JA011182

Bortnik, J., Li, W., Thorne, R. M., Angelopoulos, V., Cully, C., Bonnell, J., et al. (2009). An observation linking the origin of plasmaspheric hiss to discrete chorus emissions. *Science*, *324*(5928), 775–778. https://doi.org/10.1126/science.1171273

Bortnik, J., Thorne, R. M., & Meredith, N. P. (2007). Modeling the propagation characteristics of chorus using crres suprathermal electron fluxes. *Journal of Geophysical Research: Space Physics*, *112*(A8). https://doi.org/10.1029/2006JA012237

Bortnik, J., Thorne, R. M., & Meredith, N. P. (2008). The unexpected origin of plasmaspheric hiss from discrete chorus emissions. *Nature*, *452*(7183), 62–66. https://doi.org/10.1038/nature06741

Bortnik, J., Thorne, R. M., Meredith, N. P., & Santolik, O. (2007). Ray tracing of penetrating chorus and its implications for the radiation belts. *Geophysical Research Letters*, *34*(15). https://doi.org/10.1029/2007GL030040

Cerfolli, L., Ripoll, J.-F., Horne, R. B., Wold, A. M., & Marshall, R. A. (2025). Ray tracing of very low frequency waves produced by active experiments or lightning events at low Earth orbit. *Comptes Rendus Physique*, *26*(G1), 285–294. https://doi.org/10.5802/crphys.238

Chen, L., Bortnik, J., Thorne, R. M., Horne, R. B., & Jordanova, V. K. (2009). Three-dimensional ray tracing of vlf waves in a magnetospheric environment containing a plasmaspheric plume. *Geophysical Research Letters*, *36*(22). https://doi.org/10.1029/2009GL040451

Chen, L., Santolík, O., Hajoš, M., Zheng, L., Zhima, Z., Heelis, R., et al. (2017). Source of the low-altitude hiss in the ionosphere. *Geophysical Research Letters*, *44*(5), 2060–2069. https://doi.org/10.1002/2016GL072181

Colpitts, C., Miyoshi, Y., Kasahara, Y., Delzanno, G. L., Wygant, J. R., Cattell, C. A., et al. (2020). First direct observations of propagation of discrete chorus elements from the equatorial source to higher latitudes, using the Van Allen probes and arase satellites. *Journal of Geophysical Research: Space Physics*, *125*(10), e2020JA028315. https://doi.org/10.1029/2020JA028315

Crabtree, C., Rudakov, L., Ganguli, G., & Mithaiwala, M. (2012). Collisionless and collisional dissipation of magnetospherically reflecting whistler waves. *Geophysical Research Letters*, *39*(16). https://doi.org/10.1029/2012GL052921

Cunningham, G. S., Botek, E., Pierrard, V., Cully, C., & Ripoll, J.-F. (2020). Observation of high-energy electrons precipitated by nwc transmitter from proba-v low-earth orbit satellite. *Geophysical Research Letters*, *47*(16), e2020GL089077. https://doi.org/10.1029/2020GL089077

Ding, X., He, Z., Wu, Z., Yu, J., Li, K., Ye, Y., & Zong, Q. (2025). Radial and latitudinal distributions of the exohiss under the effect of Landau damping. *Geophysical Research Letters*, *52*(1), e2024GL112567. https://doi.org/10.1029/2024GL112567

Feng, B., Li, H., Yu, X., Yuan, Z., Tang, R., Wang, D., et al. (2023). The evolution of whistler hiss-like waves across plasmapause: Hiss to exohiss. *Geophysical Research Letters*, *50*(8), e2023GL102993. https://doi.org/10.1029/2023GL102993

Feng, B., Yu, X., Li, H., Zhou, M., Tang, R., Ouyang, Z., et al. (2025). Modeling the two-dimensional propagation of whistler-mode chorus waves in the magnetic peaks. *Journal of Geophysical Research: Space Physics*, *130*(1), e2024JA033383. https://doi.org/10.1029/2024JA033383

Ganguli, G., Crabtree, C., Fletcher, A. C., Rudakov, L., Richardson, A. S., Huba, J., et al. (2019). Understanding and harnessing the dual electrostatic/electromagnetic character of plasma turbulence in the near-earth space environment. *Journal of Geophysical Research: Space Physics*, *124*(12), 10365–10375. https://doi.org/10.1029/2019JA027372

Ganguli, G., Crabtree, C., Mithaiwala, M., Rudakov, L., & Scales, W. (2015). Evolution of lower hybrid turbulence in the ionosphere. *Physics of Plasmas*, *22*(11), 112904. https://doi.org/10.1063/1.4936281

Gombosi, T. I., Baker, D. N., Balogh, A., Erickson, P. J., Huba, J. D., & Lanzerotti, L. J. (2017). Anthropogenic space weather. *Space Science Reviews*, *212*(3–4), 985–1039. https://doi.org/10.1007/s11214-017-0357-5

Gu, W., Chen, L., Xia, Z., An, X., & Horne, R. B. (2020). Alpha transmitter signal reflection and triggered emissions. *Geophysical Research Letters*, *47*(23), e2020GL090165. https://doi.org/10.1029/2020GL090165

Gu, W., Chen, L., Xia, Z., & Horne, R. B. (2021). Direct evidence reveals transmitter signal propagation in the magnetosphere. *Geophysical Research Letters*, *48*(15), e2021GL093987. https://doi.org/10.1029/2021GL093987

Gu, W., Hartley, D., Liu, X., Chen, L., Bortnik, J., & Horne, R. B. (2024). Propagation of very oblique chorus waves near a plasmaspheric plume boundary. *Journal of Geophysical Research: Space Physics*, *129*(2), e2023JA032151. https://doi.org/10.1029/2023JA032151

Hanzelka, M., Němec, F., Santolík, O., & Parrot, M. (2022). Statistical analysis of wave propagation properties of equatorial noise observed at low altitudes. *Journal of Geophysical Research: Space Physics*, *127*(7), e2022JA030416. https://doi.org/10.1029/2022JA030416

Hanzelka, M., & Santolík, O. (2019). Effects of ducting on whistler mode chorus or exohiss in the outer radiation belt. *Geophysical Research Letters*, *46*(11), 5735–5745. https://doi.org/10.1029/2019GL083115

Hartley, D. P., Cunningham, G. S., Ripoll, J.-F., Malaspina, D. M., Kasahara, Y., Miyoshi, Y., et al. (2023). Using van allen probes and arase observations to develop an empirical plasma density model in the inner zone. *Journal of Geophysical Research: Space Physics*, *128*(3), e2022JA031012. https://doi.org/10.1029/2022JA031012

Hartley, D. P., Kletzing, C. A., Chen, L., Horne, R. B., & Santolík, O. (2019). Van allen probes observations of chorus wave vector orientations: Implications for the chorus-to-hiss mechanism. *Geophysical Research Letters*, *46*(5), 2337–2346. https://doi.org/10.1029/2019GL082111

Horne, R. B. (1988). Ray tracing of electrostatic waves in a hot plasma and its application to the generation of terrestrial myriametric radiation. *Geophysical Research Letters*, *15*(6), 553–556. https://doi.org/10.1029/GL015i006p00553

Horne, R. B. (1989). Path-integrated growth of electrostatic waves: The generation of terrestrial myriametric radiation. *Journal of Geophysical Research*, *94*(A7), 8895–8909. https://doi.org/10.1029/JA094iA07p08895

Horne, R. B., & Thorne, R. M. (1993). On the preferred source location for the convective amplification of ion cyclotron waves. *Journal of Geophysical Research*, *98*(A6), 9233–9247. https://doi.org/10.1029/92JA02972

Horne, R. B., Wheeler, G. V., & Alleyne, H. S. C. K. (2000). Proton and electron heating by radially propagating fast magnetosonic waves. *Journal of Geophysical Research*, *105*(A12), 27597–27610. https://doi.org/10.1029/2000JA000018

Huba, J. D., Joyce, G., & Krall, J. (2008). Three-dimensional equatorial spread f modeling. *Geophysical Research Letters*, *35*(10). https://doi.org/10.1029/2008GL033509

Inan, U. S., & Bell, T. F. (1977). The plasmapause as a vlf wave guide. *Journal of Geophysical Research (1896-1977)*, *82*(19), 2819–2827. https://doi.org/10.1029/JA082i019p02819

Kang, N., & Bortnik, J. (2022). Structure of energy precipitation induced by superbolt-lightning generated whistler waves. *Geophysical Research Letters*, *49*(5), e2022GL097770. https://doi.org/10.1029/2022GL097770

Kang, N., Bortnik, J., An, X., & Claudepierre, S. G. (2021). Propagation of chorus waves generated in minimum-b pockets. *Geophysical Research Letters*, *48*(24), e2021GL096478. https://doi.org/10.1029/2021GL096478

Kang, N., Bortnik, J., Ma, Q., & Claudepierre, S. (2024). Modeling the global distribution of chorus wave induced relativistic microburst spatial characteristics. *Journal of Geophysical Research: Space Physics*, *129*(3), e2023JA032250. https://doi.org/10.1029/2023JA032250

Kang, N., Bortnik, J., Zhang, X., Claudepierre, S., & Shi, X. (2022). Relativistic microburst scale size induced by a single point-source chorus element. *Geophysical Research Letters*, *49*(23), e2022GL100841. https://doi.org/10.1029/2022GL100841

Ke, Y., Lu, Q., Gao, X., Chen, H., & Chen, R. (2022). Ray-tracing simulations of whistler-mode wave propagation in different rescaled dipole magnetic fields. *Earth and Planetary Physics*, *6*(6), 555–562. https://doi.org/10.26464/epp2022048

Ke, Y., Lu, Q., Gao, X., Ma, J., Ren, J., & Zhou, X. (2025). Whistler wave propagation in a dipole magnetic field: Two-dimensional gcpic simulations. *Journal of Geophysical Research: Space Physics*, *130*(4), e2025JA033759. https://doi.org/10.1029/2025JA033759

Kimura, I. (1966). Effects of ions on whistler-mode ray tracing. *Radio Science*, *1*(3), 269–283. https://doi.org/10.1002/rds196613269

McCollough, J. P., Miyoshi, Y., Ginet, G. P., Johnston, W. R., Su, Y.-J., Starks, M. J., et al. (2022, December). Space-to-space very low frequency radio transmission in the magnetosphere using the DSX and Arase satellites. *Earth Planets and Space*, *74*(1), 64. https://doi.org/10.1186/s40623-022-01605-6

Mei, Y., Thorne, R. M., & Horne, R. B. (1992). Ion-cyclotron waves at jupiter: Possibility of detection by ulysses. *Geophysical Research Letters*, *19*(6), 629–632. https://doi.org/10.1029/92GL00400

Němec, F., Pekař, J., & Parrot, M. (2020). Nwc transmitter effects on the nightside upper ionosphere observed by a low-altitude satellite. *Journal of Geophysical Research: Space Physics*, *125*(12), e2020JA028660. https://doi.org/10.1029/2020JA028660

Phillips, J. (1987). *The nag library: A beginners guide*. Oxford University Press, Inc

Press, W. H., Teukolsky, S. A., Vetterling, W. T., & Flannery, B. P. (2007). *Numerical recipes 3rd edition: The art of scientific computing* (3rd ed.). Cambridge University Press. Retrieved from http://www.amazon.com/Numerical-Recipes-3rd-Scientific-Computing/dp/0521880688/ref=sr_1_1?ie=UTF8&s=books&qid=1280322496&sr=8-1

Reeves, G. D., Delzanno, G. L., Fernandes, P. A., Yakymenko, K., Carlsten, B. E., Lewellen, J. W., et al. (2020). The beam plasma interactions experiment: An active experiment using pulsed electron beams. *Frontiers in Astronomy and Space Sciences*, *7*, 23. https://doi.org/10.3389/fspas.2020.00023

Reid, R. A., Marshall, R. A., Starks, M. J., Usanova, M. E., Wilson, G. R., Johnston, W. R., et al. (2022). Active vlf transmission experiments between the dsx and vpm spacecraft. *Journal of Geophysical Research: Space Physics*, *127*(4), e2021JA030087. https://doi.org/10.1029/2021JA030087

Resseguier, A., Blelly, P.-L., & Marchaudon, A. (2026). A new orthogonal geomagnetic coordinate system: The generalized eccentric dipole. *Journal of Geophysical Research: Space Physics*, *131*(4), e2025JA034313. https://doi.org/10.1029/2025JA034313

Ripoll, J.-F., & Blelly, P.-L. (2026). Datasets for ray tracing in a general non-dipole magnetic field [dataset]. *Zenodo*. https://doi.org/10.5281/zenodo.20276173

Ripoll, J.-F., Claudepierre, S. G., Ukhorskiy, A. Y., Colpitts, C., Li, X., Fennell, J. F., & Crabtree, C. (2020). Particle dynamics in the earth's radiation belts: Review of current research and open questions. *Journal of Geophysical Research: Space Physics*, *125*(5), e2019JA026735. https://doi.org/10.1029/2019JA026735

Ripoll, J.-F., Farges, T., Malaspina, D. M., Lay, E. H., Cunningham, G. S., Hospodarsky, G. B., et al. (2020). Analysis of electric and magnetic lightning-generated wave amplitudes measured by the van allen probes. *Geophysical Research Letters*, *47*(6), e2020GL087503. https://doi.org/10.1029/2020GL087503

Ripoll, J.-F., Pierrard, V., Cunningham, G. S., Chu, X., Sorathia, K. A., Hartley, D. P., et al. (2023). Modeling of the cold electron plasma density for radiation belt physics. *Frontiers in Astronomy and Space Sciences*, *10*, 1096595. https://doi.org/10.3389/fspas.2023.1096595

Ripoll, J.-F., Thaller, S. A., Hartley, D. P., Cunningham, G. S., Pierrard, V., Kurth, W. S., et al. (2022). Statistics and empirical models of the plasmasphere boundaries from the van allen probes for radiation belt physics. *Geophysical Research Letters*, *49*(21), e2022GL101402. https://doi.org/10.1029/2022GL101402

Ripoll, J.-F., Thaller, S. A., Hartley, D. P., Malaspina, D. M., Kurth, W. S., Cunningham, G. S., et al. (2024). Statistics and models of the electron plasma density from the van allen probes. *Journal of Geophysical Research: Space Physics*, *129*(8), e2024JA032528. https://doi.org/10.1029/2024JA032528

Robinson, T. R., Strangeway, R., Wright, D. M., Davies, J. A., Horne, R. B., Yeoman, T. K., et al. (2000). Fast observations of ulf waves injected into the magnetosphere by means of modulated rf heating of the auroral electrojet. *Geophysical Research Letters*, *27*(19), 3165–3168. https://doi.org/10.1029/2000GL011882

Sauvaud, J.-A., Maggiolo, R., Jacquey, C., Parrot, M., Berthelier, J.-J., Gamble, R. J., & Rodger, C. J. (2008). Radiation belt electron precipitation due to vlf transmitters: Satellite observations. *Geophysical Research Letters*, *35*(9). https://doi.org/10.1029/2008GL033194

Schmidt, E. (1907). Zur theorie der linearen und nichtlinearen integralgleichungen. i. teil: Entwicklung willkürlicher funktionen nach systemen vorgeschriebener. *Mathematische Annalen*, *63*, 433–476. Retrieved from http://eudml.org/doc/158296

Starks, M. J. (2002). Effects of hf heater-produced ionospheric depletions on the ducting of vlf transmissions: A ray tracing study. *Journal of Geophysical Research: Space Physics*, *107*(A11). https://doi.org/10.1029/2001JA009197

Starks, M. J., Albert, J. M., Ling, A. G., O'Malley, S., & Quinn, R. A. (2020). Vlf transmitters and lightning-generated whistlers: 1. modeling waves from source to space. *Journal of Geophysical Research: Space Physics*, *125*(3), e2019JA027029. https://doi.org/10.1029/2019JA027029

Starks, M. J., Quinn, R. A., Ginet, G. P., Albert, J. M., Sales, G. S., Reinisch, B. W., & Song, P. (2008). Illumination of the plasmasphere by terrestrial very low frequency transmitters: Model validation. *Journal of Geophysical Research: Space Physics*, *113*(A9). https://doi.org/10.1029/2008JA013112

Suchy, K. (1981). Real Hamilton equations of geometric optics for media with moderate absorption. *Radio Science*, *16*(6), 1179–1182. https://doi.org/10.1029/RS016i006p01179

Swanson, D. G. (2003). Plasma waves. *Series in Plasma Physics*. https://doi.org/10.1201/9780367802721.2nd ed.

Thorne, R. M., & Horne, R. B. (1994). Landau damping of magnetospherically reflected whistlers. *Journal of Geophysical Research*, *99*(A9), 17249–17258. https://doi.org/10.1029/94JA01006

Thorne, R. M., Ni, B., Tao, X., Horne, R. B., & Meredith, N. P. (2010). Scattering by chorus waves as the dominant cause of diffuse auroral precipitation. *Nature*, *467*(7318), 943–946. https://doi.org/10.1038/nature09467

Tsyganenko, N. (1989). A magnetospheric magnetic field model with a warped tail current sheet. *Planetary and Space Science*, *37*(1), 5–20. https://doi.org/10.1016/0032-0633(89)90066-4

Usanova, M. E., Reid, R. A., Xu, W., Marshall, R. A., Starks, M. J., & Wilson, G. R. (2022). Using vlf transmitter signals at leo for plasmasphere model validation. *Journal of Geophysical Research: Space Physics*, *127*(4), e2022JA030345. https://doi.org/10.1029/2022JA030345

Wold, A. M., Marshall, R. A., Malaspina, D. M., & Shane, A. D. (2024). Prevalence and propagation of lightning-generated whistlers in van allen probes efw burst data. *Journal of Geophysical Research: Space Physics*, *129*(9), e2024JA032781. https://doi.org/10.1029/2024JA032781

Wu, Z., Su, Z., Zheng, H., Wang, Y., Miyoshi, Y., Shinohara, I., et al. (2024). Long lifetime hiss rays in the disturbed plasmasphere. *Geophysical Research Letters*, *51*(4), e2023GL107825. https://doi.org/10.1029/2023GL107825

Xia, Z., Chen, L., Horne, R. B., & Bortnik, J. (2022). Whistler waves above the lower hybrid frequency in the ionosphere and their counterparts in the magnetosphere. *Geophysical Research Letters*, *49*(8), e2022GL098294. https://doi.org/10.1029/2022GL098294

Xia, Z., Chen, L., Horne, R. B., Liu, X., He, J., & Bortnik, J. (2024). On the wave-normal distribution of lightning-generated whistlers and their propagation modes. *Journal of Geophysical Research: Space Physics*, *129*(4), e2023JA032353. https://doi.org/10.1029/2023JA032353

Xu, X., Zhou, C., Chen, L., & Horne, R. B. (2023). Modeling the propagation of fast magnetosonic waves and their conversion to electromagnetic ion cyclotron waves at low l shells. *Journal of Geophysical Research: Space Physics*, *128*(9), e2022JA031271. https://doi.org/10.1029/2022JA031271

Yabroff, I. (1959). *Computation of whistler ray paths*. Stanford Research Institute.

Yue, C., Chen, L., Bortnik, J., Ma, Q., Thorne, R. M., Angelopoulos, V., et al. (2017). The characteristic response of whistler mode waves to interplanetary shocks. *Journal of Geophysical Research: Space Physics*, *122*(10), 10047–10057. https://doi.org/10.1002/2017JA024574

Zhang, Z., Chen, L., Li, X., Xia, Z., Heelis, R. A., & Horne, R. B. (2018). Observed propagation route of vlf transmitter signals in the magnetosphere. *Journal of Geophysical Research: Space Physics*, *123*(7), 5528–5537. https://doi.org/10.1029/2018JA025637